Topological Materials for Functional Optoelectronic Devices

Hamid Chorsi,* Bing Cheng, Bo Zhao, Johann Toudert, Viktar Asadchy, Omor F. Shoron, Shanhui Fan, and Ryusuke Matsunaga

The recent realization of topology as a mathematical concept in condensed matter systems has shattered Landau's widely accepted classification of phases by spontaneous symmetry breaking as he famously said, "a particular symmetry property exists or does not exist." Topological materials (TMs) such as topological insulators and topological semimetals, are characterized by properties that depend on the topology of the band structure. Such dependence has drastic implications on the optical, electrical, and thermal properties of the material. Fundamental physics of TMs is currently under active research in condensed matter, materials science, and high energy physics. In this review, recent advances in exploiting the unique properties of TMs to realize functional optoelectronic devices are surveyed. Current and future applications that are, or may be, enabled by their unique properties are discussed. Although many theoretical ideas have been proposed over the past decade or so on using TMs in optoelectronic applications, the focus will be on experimentally realized devices.

1. Introduction

Endeavors to unearth the mystery of the quantum Hall state with insulating bulk and conducting surface states have paved the way for the entrance of topology in condensed matter physics and material science. Topological materials (TMs) are materials in which the topological aspects of the electronic band structure, typically includes boundary effects such as surface states, largely alter the optical, electrical and thermal properties of the material. Comprehensive review of early theoretical and material development of TMs can be found in several review articles.[1–7] Understanding the implication of topology on the physical properties of TMs is under intense research in condensed matter physics, high-energy physics, materials chemistry, materials science, and biophysics. Such perception is expected to have central impact on using TMs in technological applications such as nanophotonics, topological quantum computing, topological spintronics, and topological photonics to name a few. Although most experimental studies on TMs so far have mainly focused on the transport, angle-resolved photoemission spectroscopy (ARPES), terahertz spectroscopy, and momentum-resolved photoelectron microscopy to investigate the physical properties of the material, new directions are emerging to exploit unique properties of these materials in optoelectronic devices. This along with fundamental study of TMs and material development can unleash the potential of TMs in realizing improved optoelectronic devices.

In this review, we discuss recent advances in functional optoelectronic devices based on TMs. We start with a brief review of the most recent advances in topological transistors. Although the focus of this review is on optoelectronic devices, transistors as the most prevalent electronic devices have had profound influence on analog and digital technological advancements.

H. Chorsi
Department of Electrical and Computer Engineering
University of California
Los Angeles, CA 90024, USA
E-mail: hchorsi@ucla.edu
B. Cheng
Stanford Institute for Materials and Energy Sciences
SLAC National Accelerator Laboratory and Stanford University
Menlo Park, CA 94025, USA
B. Zhao,[+] V. Asadchy, S. Fan
Department of Electrical Engineering
Stanford University
Ginzton Laboratory, Stanford, CA 94305, USA

(iD) The ORCID identification number(s) for the author(s) of this article can be found under https://doi.org/10.1002/adfm.202110655.

[+]Present address: Department of Mechanical Engineering, University of Houston, TX, 77204, USA

J. Toudert
ENSEMBLE3 Centre of Excellence
Wolczynska 133, Warsaw 01919, Poland
O. F. Shoron
University of California
Santa Barbara, CA 93117, USA
R. Matsunaga
Institute for Solid State Physics
University of Tokyo
Kashiwa 113-0033, Japan
R. Matsunaga
PRESTO
Japan Science and Technology Agency
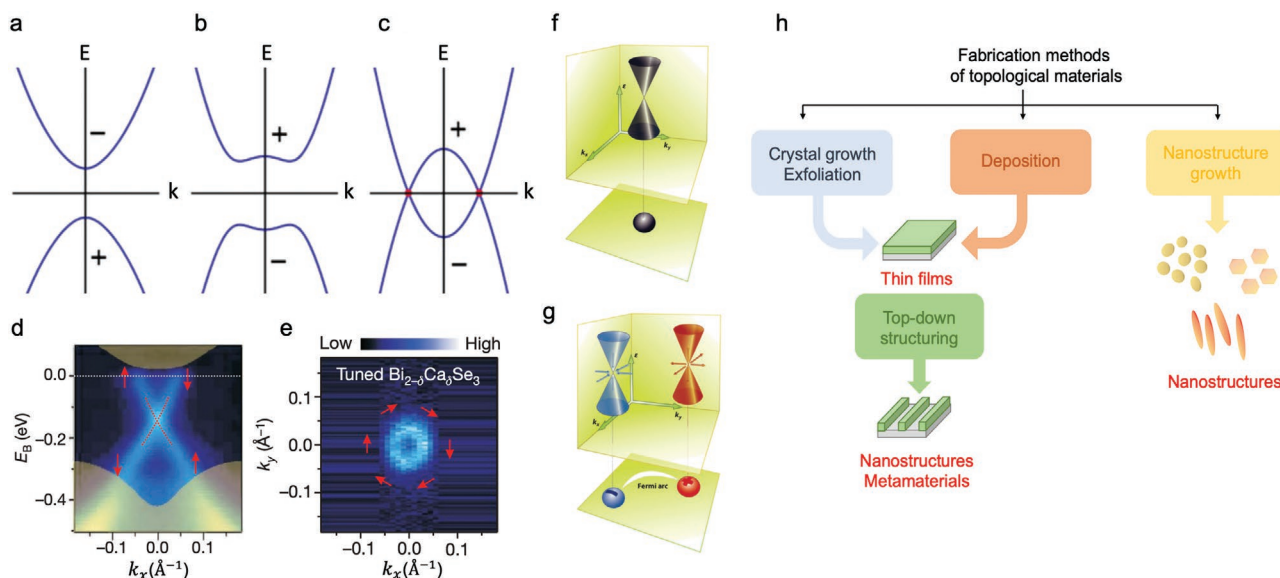Saitama 332-0012, Japan

Figure 1. Figure 1. Fundamentals and synthesis of TMs. a) Schematic of the band structure of semiconductors in which the conduction and valance bands are aligned in normal order. b) Schematic of the band structure of semiconductors in which the conduction and valance bands are inverted due to SOC. c) Schematic of the band structure of topological semimetals in which the conduction and valance bands are inverted due to SOC, but the band crossings still remain at discrete points in k space due to lattice symmetries. (Reproduced with permission.[7] Copyright 2018, American Physical Society). d) The linear band dispersion of topological surface states in a TI $Bi_{2-\delta}Ca_\delta Se_3$. e) The spin texture of topological surface states in a TI $Bi_{2-\delta}Ca_\delta Se_3$. (Reproduced with permission.[8] Copyright 2015, IOP Publishing). f) Schematic of the band structure of Dirac semimetal. Because of the time-reversal and inversion symmetries, the 3D Dirac cone is twofold degenerate. g) Schematic of the band structure of Weyl semimetal in which either time-reversal symmetry or inversion symmetry is broken. The twofold degenerate Dirac cone is split to a pair of nondegenerate Weyl cones. (Reproduced with permission.[9] Copyright 2017, Annual Reviews). h) Schematic representation illustrating various approaches used for the synthesis of TMs.

Besides, grasping the essential concepts of topological transistors grants principal means and notions for exploiting TMs in several applications and functional devices. We then survey recent advances in harnessing TMs in PDs. Current infrared detectors based on HgCdTe and InAs are bulky, power hungry, expensive, and require cryogenic cooling. Results from recent literature on TM-based PDs show promising results in realizing compact and room temperature infrared detectors. Afterward, we review nanophotonic and plasmonic devices that exploit the outstanding optoelectronic properties of TMs. As a blossoming research area, TM-based thermal and nonreciprocal devices are opening opportunities in heat transfer and energy conversion. We provide the fundamental concepts and review recent developments in topological thermal devices. Finally, we end our review with introducing recent progresses in nonlinear optics of TMs. Because of the 2D or 3D linear band dispersion, strong light could drive large nonlinear intraband currents or create unique nonequilibrium electron distributions in TMs. Therefore, TMs are promising material systems for high harmonic generations and saturable absorbers. We further discuss the possibility to realize stimulated emission in TMs. These progresses are important to develop next-generation laser sources in mid/far-infrared and terahertz (THz) region.

2. Fundamental Properties and Synthesis of TMs

The studies of topology in condensed matter have given a new classification scheme of matter phase without considering any symmetry breaking.[5,6] A striking consequence of topology in matter manifests itself in electronic properties at the surface

or interface of the materials. A famous example is topological insulators (TIs), which are nominally insulating materials in their bulk properties, but also host conductive states localized at the surface (edge) of 3D (2D) TIs.[10–12] In contrast to normal semiconductors where the valence and conduction bands are composed of electrons with p and s orbitals (**Figure 1**a), respectively, the strong spin-orbit coupling (SOC) in TIs results in the band inversion with p-like conduction and s-like valence band (Figure 1b). Such a peculiarity of the band structure can be characterized by a Z_2 topological invariant.[10] The nontrivial topological invariant in TIs does not allow a smooth connection to topologically trivial entities such as the vacuum and normal semiconductors, and therefore gives rise to surface (or edge) states connecting the bulk valence and conduction bands. The conductive surface state shows intriguing transport properties because of the spin-momentum locking,[13] that is, the spin degree of freedom is fixed with the momentum of electrons as shown in Figure 1e. Therefore, the wave functions of two electron states moving forward and backward cannot mix due to their different spin states, which results in the band crossing of the surface states. The energy dispersion around the band crossing points is linear to the momentum (Figure 1d), in contrast to the parabolic dispersion in usual materials, and the crossing point is called the Dirac nodes because the electrons no longer obey the Schrödinger equation and behave as massless particles described in the relativistic Dirac equation.[12] Such massless Dirac fermions also appear in graphene, an atomic monolayer honeycomb carbon sheet.[14] In contrast to the Dirac nodes in graphene which can be easily removed by SOC,[15] the existence of the Dirac surface state of TIs is "topologically-protected" and therefore highly robust against perturbations.[10]

The spin-momentum locking also prohibits backscattering, which results in a weak anti-localization behavior in magneto transport and potentially allows a highly ballistic transport of electrons.[16] As a counterpart of TIs, topological crystalline insulators (TCIs) also host surface states.[17] However, the surface states in TCIs are protected by lattice symmetries rather than time-reversal symmetry. SnTe is the most famous representative of TCIs, whose surface states are protected by lattice mirror symmetry. One can define a new topological invariant called mirror Chern number to classify whether a material is topologically trivial or nontrivial if it preserves lattice mirror symmetry.[18] The surface states in TIs and TCIs share common features and most arguments applied in TIs are still valid in TCIs.

While the Dirac fermions in TIs and TCIs are localized at their surfaces, recently the emergence of the massless fermions in 3D bulk states have attracted more attention in materials called topological Dirac semimetals (TDSs) and topological Weyl semimetals.[7] Na_3Bi and Cd_3As_2 are two well-known representatives of TDSs;[19,20] they host band inversions like TIs, but their bulk bandgap is not fully open. The band crossings remain at two spots along the kc axis due to rotational symmetry around the c axis (Figure 1c). Therefore, as shown in Figure 1f, the 3D linear band dispersions appear in the bulk state around the symmetry-protected Dirac nodes and behaves as 3D analogue of graphene. Note that the Dirac nodes have a fourfold degeneracy because of the inversion and time-reversal symmetries. If either is broken, as shown in Figure 1g, the fourfold degeneracy of the nodes is lifted, resulting in a pair of twofold degenerate Weyl nodes separated by a finite momentum in momentum space.[7] The Weyl nodes always appear in pairs with opposite chiralities, and play roles of source and sink of Berry curvature which could be regarded as effective magnetic monopole and anti-monopole in momentum space.[21,22] Many magnetic materials with broken time-reversal symmetry can host many Weyl nodes in their Brillouin zone.[23,24] When the Weyl nodes exist near the Fermi level and there are no other metallic bands, the nature of Weyl semimetals can emerge in their transport. For nonmagnetic materials, TaAs and WTe_2 are well known examples of Weyl semimetal with broken inversion symmetry, which allows second-order nonlinear optical responses such as rectification and frequency mixing.[21,25]

To drive the development of TM-based optoelectronic devices, reliable and reproducible fabrication techniques are crucial. Crystal growth techniques combined with exfoliation are practical and cheap ways of producing thin films with a controlled composition, but the film area is limited by that of the exfoliated crystal. Wider areas, a finely tuned thickness, and a strong binding to substrates can be obtained by thin film growth techniques, which are however more costly and need specific substrates. Nanostructures can be grown by a wide range of low-cost large-scale techniques, which do not yet enable the accuracy needed for metamaterial production. Such accuracy is enabled by lithographic top-down structuring, which is however limited to small areas and costly (Figure 1h). Current challenges aim at achieving large-area metamaterials with low-cost methods. A summary of the state-of-the-art fabrication methods for TMs is provided in Appendix 1.

3. Field Effect Transistors

Unique electronic and spin properties can improve transistor performance drastically and enable it with new characteristics. The lack of backscattering in TMs due to chirality can be used to design transistors with high current density and transconductance, which are important for RF application. The unique electronic band structure of TMs can offer unique characteristics in TM channel field effect transistors (FETs). For example, FETs based on traditional semiconductors suffer from a "density-of-states (DOS) bottleneck" due to a trade-off between mobility and density of states.[26] High mobility semiconductors usually have a very low DOS due to a low effective mass, and this results in a low current density and a large sheet resistance in FETs. The high-frequency performance of traditional FETs is severely affected by this large resistance. On the other hand, the DOS of TMs is tunable because of the linear energy dispersion. Moreover, most of the TMs have multiple Dirac nodes, which further increase the DOS. Thus, a TM-based channel FET has the potential to overcome the "DOS bottleneck" of the traditional FETs. Furthermore, constant carrier velocity (Fermi velocity) in Dirac bands of TMs can ensure linearity in current cut-off frequency and transconductance, which is important for RF circuit designing.[27]

Even though TMs are a new class of materials, significant experimental progress has been reported in TM channel FETs. Novel device structures with TIs or 3D TDS channels have shown promising results. In this section, we will review the recent progress of FETs with TI (Bi_2Te_3, Bi_2Se_3) and TDS (Cd_3As_2) as channel materials. A summary of major advances in the field is provided in **Table 1**.

Xiu et al. have demonstrated the modulation of surface state carriers in Bi_2Te_3 nanoribbon by fabricating a FET.[28] The schematic diagram of the device is shown in **Figure 2**a. The nanoribbon has a width of about 185 nm, channel length of 2 mm and thickness of 30 nm. The topological properties of TIs remain for a thickness down to few quintuple layers (less than 10) where the bulk bandgap widens[31,32] Figure 2b shows the modulation of the conductance of Bi_2Te_3 nanoribbon. The conductivity modulation of this device is very low, around 20% at 1.4 K, and the modulation degrades at higher temperatures. Low bulk bandgap in Bi_2Te_3 (0.14 eV) is the main reason behind this low modulation. Figure 2c shows the Fourier transformation of the SdH oscillation. This result shows a steady left shift of the peak of the surface states (indicated by arrows) at negative gate voltage, indicating a depletion of surface state carriers with negative voltage. But the peaks due to bulk carriers (green circles) show an increase in bulk carrier density because of hole accumulation at negative gate voltage. This ambipolar transport is another reason for poor modulation performance in this device.

Several groups have reported different techniques to improve the current modulation of Bi_2Te_3 FETs. H. Liu et al. have demonstrated dual gated Bi_2Te_3 channel FET (Figure 2d) to improve current modulation.[29] Figure 2e shows the current modulation of Bi_2Te_3 device with a dual gate. This dual gate structure shows maximum current modulation of 76% at room temperature. But, the effect of the top gate is very poor due to bad interface quality. On the other hand, Yan et al. have used ferroelectric $0.71Pb(Mg_{1/3}Nb_{2/3})O_3$-$0.29PbTiO_3$ (PMN-PT) as a gate insulator and have used the nonvolatile polarization direction of

ADVANCED
SCIENCE NEWS
www.advancedsciencenews.com

ADVANCED
FUNCTIONAL
MATERIALS
www.afm-journal.de

Table 1. Major advances in the realization of topological transistors and surface state modulation (MBE: molecular beam epitaxy, CVD: chemical vapor deposition, TI: topological insulator, TDS: topological Dirac semimetal).

| Material	Bandgap	Structure	Mechanism	Gating method	Phase	Year	Reference
Bi_2Se_3	0.3 eV (bulk)	Thin film (<100 nm)	Exfoliated	Back-gated/ top-gated	TI	2010	[38]
Bi_2Se_3	0.3 eV (bulk)	Quintuple layer	Exfoliated	Back-gated	TI	2011	[33]
Bi_2Te_3	0.14 eV (bulk)	Thin film	Exfoliated	Back-gated/ top-gated	TI	2011	[29]
Bi_2Te_3	0.14 eV (bulk)	Nanoribbons	Suspension	Back-gated	TI	2011	[28]
Bi_2Te_3	–	Na-doped nanoplates	Solvo-thermal	Back-gated	TI	2012	[39]
Bi_2Se_3	0.3 eV	Nanowire	Solid–vapor–solid route	Surrounding-gated	TI	2013	[34]
$Cr_{0.15}(Bi_{0.1}Sb_{0.9})_{1.85}Te_3$	–	Thin film	MBE	Top-gated	TI	2014	[40]
$(Bi_{1-x}Sb_x)_2Se_3$	–	Thin film	MBE	Back-gated	TI	2017	[36]
Ni_3Bi	0.3 eV (bulk)	Few-layer	MBE	Metallic tip	TI	2018	[41]
Bi_2Se_3	0.3 eV (bulk)	Nanowire	CVD	Surrounding-gated	TI	2019	[35]
Cd_3As_2	0 eV (bulk)	Thin film	MBE	Back-gated	TDS	2019, 2020	[27, 37]
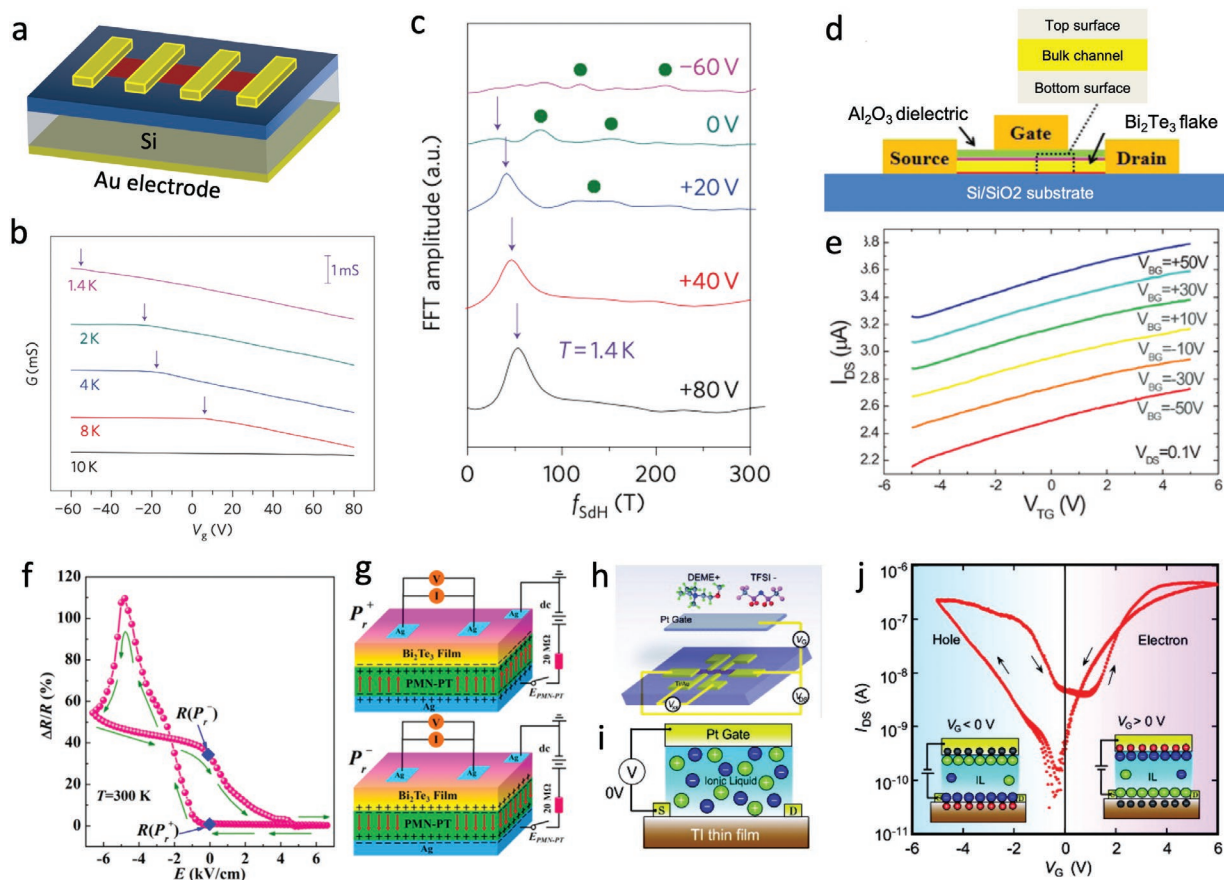
Figure 2. TMs as a channel of a FET. a) Schematic diagram of back gated Bi_2Te_3 nanoribbon FETs. b) Channel conductivity as a function of gate voltage and c) Fourier transform of SdH oscillation in Bi_2Te_3 nanoribbon at different gate voltage. Reproduced with permission.[28] Copyright 2011, Springer Nature. d) Schematic diagram of a dual gated Bi_2Te_3 FETs and e) its I_D–V_{TG} characteristics for different back gate voltages. Reproduced with permission.[29] Copyright 2011, American Institute of Physics. f) Change of channel resistance in a ferroelectric gated Bi_2Te_3 FET. g) Schematic diagram of the ferroelectric gated FETs. Reproduced with permission.[30] Copyright 2019, American Chemical Society. h) Top and i) cross section view of liquid ion gated Bi_2Te_3 FET and j) its I_D–V_g characteristics at 220 K. Reproduced with permission.[42] Copyright 2011, American Chemical Society.

**ADVANCED
SCIENCE NEWS**

www.advancedsciencenews.com

**ADVANCED
FUNCTIONAL
MATERIALS**

www.afm-journal.de

ferroelectric PMN-PT to modulate Fermi level and sheet carrier density of epitaxial Bi_2Te_3 thin film.[30] Bi_2Te_3 film was grown on PMNPT substrate to fabricate back gated FETs, as shown in Figure 2g. Figure 2f shows the change of channel resistance as a function of an applied electric field. A hysteresis in channel resistance is visible due to ferroelectric gating, and more than 100% change in channel resistance is possible by this technique at room temperature. Recently, H. Yuan et al. have used the ionic liquid to gate Bi_2Te_3 FETs, as shown in Figure 2h,i. Molecular beam epitaxy was used to grow ultra-thin Bi_2Te_3 film.[42] Due to this extreme thickness a bandgap opens up, and the film becomes semiconducting with a bandgap of 0.48 eV. Due to semiconducting nature of the film, this device shows an on/off ratio of over 10^3, as shown in Figure 2j.

To improve current modulation in TI channel FETs, a wider bulk gap is needed. Bi_2Se_3 has a wider bulk gap (0.3 eV) compared to Bi_2Te_3 and hence shows better FET performance. Cho et al. have demonstrated back gated FETs using exfoliated Bi_2Se_3 as shown in **Figure 3**a.[33] Figure 3b shows the channel resistance as a function of gate voltage. The thick Bi_2Se_3 channel devices show a low change in channel resistivity (20–50%). But very thin channel device (3.5 nm) shows complete turn-off at 1.4 K. On the other hand, H. Zhu et al. have fabricated and characterized Bi_2Se_3 nanowire channel FETs.[34] The cross-section of the device is shown in Figure 3c. The device shows a sharp turn-on and large current saturation with an on/off ratio of over 1000 at 77 K, as shown in Figure 3d. But on/off ratio degrades significantly (≈10) near room temperature. The saturation current of this device does not follow the conventional quadratic relationship of long channel device. Instead, saturation current shows a linear dependence on the overdrive voltage. This dependence suggests that the saturation is achieved due to the saturation velocity of the carriers, not because of pinch-off at the drain end of the channel.

Enhancement mode Bi_2Se_3 nanowire FETs also show anomalous Aharonov–Bohm (AB) oscillation under strong surface disorder, as shown in Figure 3e,f.[35] This anomalous AB oscillation indicates carrier transport along the nanowire surface perimeter. Moreover, the period of the oscillations depends on the gate voltage, indicating the conduction channel quantization at the surface. Lately, Y-H. Liu et al. have demonstrated FET with ternary TI, $(Bi_{1−x}Sb_x)_2Se_3$.[36] molecular beam epitaxy (MBE) grown $(Bi_{1−x}Sb_x)_2Se_3$ channel FET shows 25 000% modulation in channel resistance when channel thickness is 5 nm, as shown in Figure 3g,h. This enhanced resistance modulation arises from decreased film thickness and Sb doping. Doping Bi_2Se_3 with Sb and In is anticipated to lower the bulk bandgap.[43]

A recent addition to the TM system is 3D TDSs. There are several reports of FETs with 3D TDS Cd_3As_2 channel. Cd_3As_2 has extreme high Fermi velocity, higher than the Fermi velocities of any other TMs or saturation velocities of any semiconductors.[37] As a result, Cd_3As_2 channel FETs exhibit extreme high current density.[27,37] It should be noted that although 3D TDSs do not have a bulk bandgap, recent studies indicate that the Dirac nodes become gapped in extremely thin (below 60 nm) films.[44–46] Shoron et al. have demonstrated ambipolar transport in MBE grown Cd_3As_2 channel FETs at low temperature, as shown in Figure 3i,j.[37] Nonetheless, the current modulation at room temperature degrades because of large bulk carrier density and interface trap densities. Modified narrow channel FET (Figure 3k)

shows much better room temperature performance.[27] Figure 3l shows that narrow channel Cd_3As_2 FET exhibits extreme high current density, as high as 4 A mm^{-1}. Moreover, this device shows peak transconductance of 120 mS mm^{-1} with a room temperature current modulation of over 25%. Much higher current modulation (>50%) has been demonstrated in a longer channel FET.

4. Photodetectors

A photodetector (PD) is generally referred to any tool that is capable of detecting optical radiation. PDs exploit light-induced material effects that can be measured via electrical signals to sense the incoming electromagnetic radiation. Considering such a definition, many semiconductors with the optical bandgap in the radiation range can be exploited to detect the incident photons. PDs have been drastically improved over the past 50 years and are presently under progress and advancement. Nevertheless, several key bottlenecks (mostly originating from the constituent material) hinder their overall figures of merit (see Box 1). Areas that need further research include room temperature operating devices, broadband detectors covering visible, infrared, and even longer wavelengths and reducing the device footprint for applications in miniaturized and integrated photonic applications. Such improvements can have drastic implications in many areas of science including medical imaging, low-light imaging, portable and flexible apparatus, and quantum optics to name a few. Besides, unlike semiconductor-based photodetectors for visible and near-infrared regions, many conventional semiconductor-based photodetectors for mid-infrared such as HgCdTe and PbS are limited by dark currents generated via thermal carriers at room temperature. Graphene photodetectors have shown promising results for room temperature operation. Unfortunately, single layer graphene has low absorption efficiency, about 2.3% per layer, which limits its conversion efficiency and constrains room temperature operation.

Box 1: Key Characteristics of a Photodetector

The key terms of merit for characterizing a photodetector's performance are defined below.

Responsivity: The responsivity of a detector (R) is the ratio of the electric current (I) flowing in the circuit to the incident optical power (P), that is, $R = I/P$, (AW^{-1}).

Specific Detectivity: Specific detectivity (D^*) is related to the inverse of the smallest radiant that can be detected (NSD). D^* is expressed as $D^* = R \times \sqrt{A}/\text{NSD}$, (cm Hz$^{1/2}$ W^{-1}), where A is the active area.

Photo-Gain: Photo-gain (G) represents the number of the generated charge carriers per single incident photon. G is defined as $G = T/T_{tr}$, where T is the carrier lifetime and T_{tr} is the carrier transit time between the contacts.

On/Off Ratio: On/off ratio (OOR) quantifies the ratio of the current with light ON to the current with light OFF.

Response Time: PDs exhibit different transient behavior. Response time is the time required for charge carrier saturation after the light is turned on.
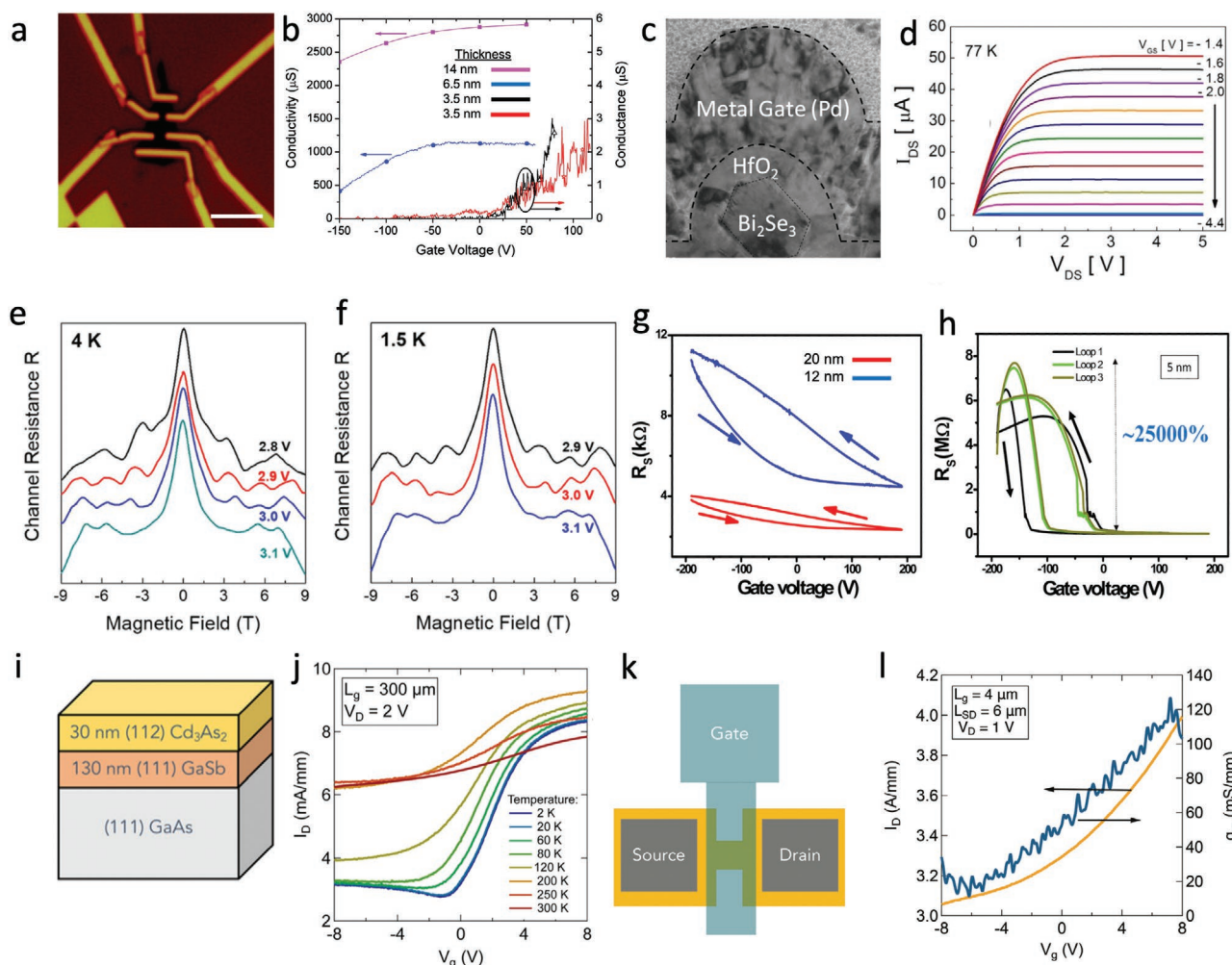
Figure 3. Bi_2Se_3 and Cd_3As_2 channel FETs. a) Top view of exfoliated Bi_2Se_3 FETs with back gate, b) Change of channel resistance of exfoliated Bi_2Se_3 with gate voltage for different channel thickness. Reproduced with permission.[33] Copyright 2011, American Chemical Society. c) Cross section image of Bi_2Se_3 nanowire FET and d) its ID–VD characteristics at 77K. Reproduced with permission.[34] Copyright 2013, Springer Nature. e,f) Magnetoresistance of Bi_2Se_3 nanowire FETs for 4 and 1.5 K, respectively. Reproduced with permission.[35] Copyright 2019, American Institute of Physics. g,h) Modulation of channel resistance in ternary $(Bi_{1-x}Sb_x)_2Se_3$ channel FET for different channel thicknesses. Reproduced with permission.[36] Copyright 2017, American Chemical Society. i) Epitaxial structure of Cd_3As_2 channel FETs. j) I_D–V_g characteristics of long channel Cd_3As_2 FET at different temperature ranging from 2 to 300 K. Reproduced with permission.[37] Copyright 2019, American Institute of Physics. k) Schematic diagram of modified narrow channel Cd_3As_2 FET, and l) its I_D–V_g and transconductance characteristics at room temperature. Reproduced with permission.[27] Copyright 2020, Wiley-VCH.

TMs with their unique properties that originate from their band structure can be used to improve upon current PDs. Ultrafast charge carrier dynamics and broadband response due to linear dispersion in TIs can be deftly exploited to obtain ultra-broadband, high speed, and high-quantum-efficiency PDs. Besides, tunable surface bandgap and polarization-sensitive photocurrent could find applications in tunable optical devices. Furthermore, TDSs and Weyl semimetals have demonstrated to have high responsivity as a result of linear dispersion and suppressed back scattering. It has been also shown that optical response of several TMs can be widely tuned externally.[52] Generally speaking, there are multiple ways to generate detectable photocurrents. The conventional approach in semiconductor-based detectors includes current generation due to the built-in electric fields present in p-n junctions. Recently, an alternative approach was suggested based on the bulk photovoltaic (photogalvanic) effect,[53–56] which is a nonlinear phenomenon of the second order corresponding to the optical

rectification. The advantages of this approach include an ultrafast response due to the direct acceleration of the charge carriers as well as the absence of the standard limitations on the efficiency (such as the detailed balance limit applicable for p-n junctions in solar energy harvesting). However, the main disadvantage precluding device implementation based on the bulk photovoltaic effect is the weak amplitude of nonlinear effects in conventional materials. On the other hand, novel TMs have demonstrated colossal enhancement of the effect, making it technologically attractive for photodetection.[57] Material candidates to probe this effect include the type-I Weyl semimetal TaAs family.[58] At present, the bulk photovoltaic effect is understood in the frameworks of nonlinear optics[59] and topology.[55,57] It occurs in the bulk and requires noncentrosymmetric material structure (broken inversion symmetry). Thus, in 2D Dirac materials, such as graphene, this effect is forbidden by symmetry.[57] In contrast, Weyl semimetals with broken inversion symmetry can host nonlinear photocurrents.
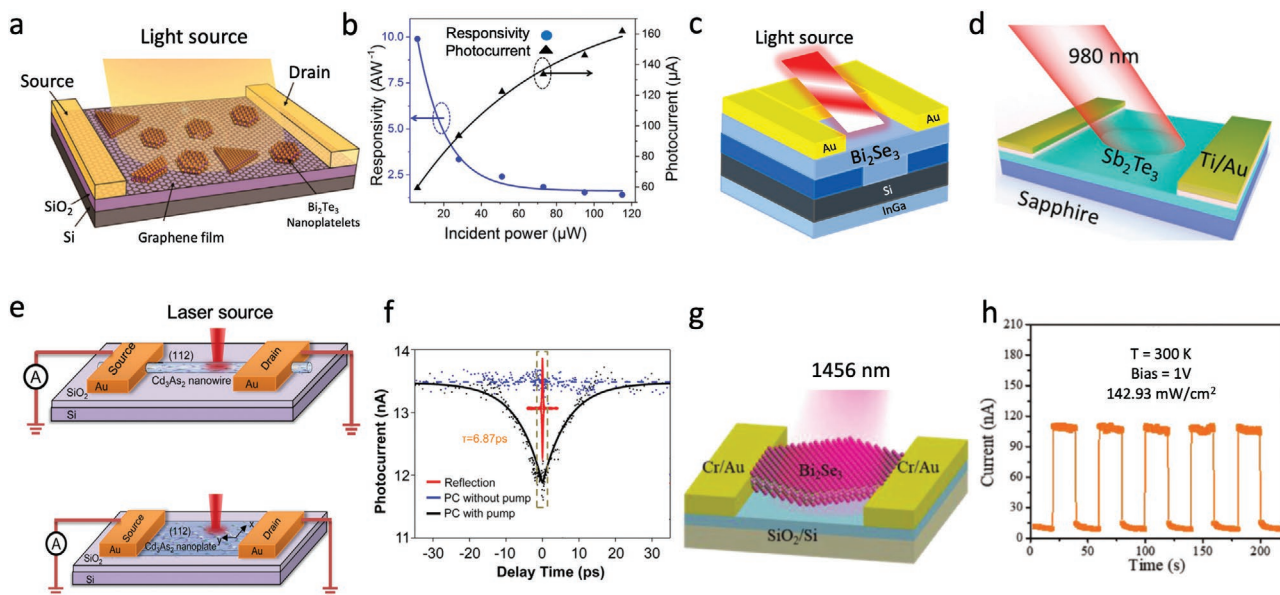
**ADVANCED
SCIENCE NEWS**

www.advancedsciencenews.com

**ADVANCED
FUNCTIONAL
MATERIALS**

www.afm-journal.de

Figure 4. TMs for photodetecting applications. a) Schematic of the Bi_2Te_3-graphene heterojunction. b) Responsivity and photocurrent for the device shown in (a). Reproduced with permission.[47] Copyright 2015, American Chemical Society. c) Schematic showing a Bi_2Se_3/Silicon heterostructure photodetector with Au top electrode. d) Sb_2Te_3 PD under 980 nm excitation. Reproduced with permission.[48] Copyright 2015, Royal Society of Chemistry. e) Schematic illustration of the nanowire and nanoplate based on the TDS Cd_3As_2. f) Pump–probe study of photoresponse as a function of time-delay with pump being ON (black) and pump being OFF (blue). Reproduced with permission.[50] Copyright 2017, American Chemical Society. g) Schematic of the back-gated Bi_2Se_3 device under the 1456 nm infrared radiation. The realized device was fabricated using EBL. h) Photoresponse of the 2D Bi_2Se_3 PD under the radiation of 142.93 mW cm^{-2}. Reproduced with permission.[51] Copyright 2018, Wiley-VCH.

The origins of the DC (direct current) photocurrent due to the bulk photovoltaic effect are classified into three groups: due to "injection" (same as "circular photocurrent"),[57,65–71] "shift,"[58,70,72] and "anomalous"[73–76] contributions. The circular photocurrent can only occur in response to circularly polarized light and it flips the sign together with the helicity of light. The mechanism of the circular photocurrent generation on the example of Weyl semimetals can be understood based on the topological description.[57,67] Consider Weyl semimetal with band structure containing two nondegenerate Weyl nodes with opposite chirality which lie at different energy levels, with the first node well below and the second node in the vicinity of the Fermi surface. Since the nodes have opposite chirality, they would generate opposite sense of photocurrent. However, excitations of the first node by low-energy photons are blocked due to Pauli exclusion principle (excited electrons have energies below the Fermi energy), and a photocurrent is generated only by the second node.[67] At the second Weyl node the circularly polarized photons will excite electrons of only one spin due to the chirality selection rule, which is the result of the angular momentum conservation. Since the spins of the electrons are locked to their momentum directions, the photocurrent generated by the second Weyl node will flow unidirectionally, and the net current will be nonzero. An alternative mechanism of photocurrent generation is based on tilted Weyl nodes which occurs in type-II Weyl semimetals.[57] In realistic semimetals, such as TaAs and CoSi, the circular photocurrent can reach values of the order of 500 μAV^{-2} (see refs. [58, 66, 77]), which significantly exceeds that in other chiral crystals.

In the absence of electron scattering, the circular photocurrent would grow linearly in time since its time derivative dJ/dt has a constant value.[59] In realistic materials, the scattering cannot be neglected and the photocurrent reaches some satura-

tion DC value. On the contrary, the shift photocurrents[58,70,72] are generated due to the linear displacement of electrons when they undergo an optical transition. The shift currents are DC even in the absence of scattering,[59] and therefore, they are more pronounced than circular photocurrents in the cases of short relaxation times.[58] The shift current emerge only from the excitation by linearly polarized light. The anomalous contribution to the DC photocurrent stems from the anomalous velocity, which is controlled by the Berry curvature of Weyl semimetals.[73–76] The anomalous photocurrent is a DC current even in the absence of electron scattering and can be generated only by circularly polarized light.[74]

In a pioneering work Qiao et al.[47] exploited graphene-Bi_2Te_3 heterostructure to realize a broadband detector with photoresponsivity as high as 35 AW^{-1} and photoconductive gain up to 83. The integration of low-bandgap TI with zero bandgap graphene extended the operating wavelength of integrated PD to near-infrared region while maintaining the high mobility of graphene. The similar hexagonal symmetry between graphene and Bi_2Te_3 allowed epitaxial growth of Bi_2Te_3 nanocrystals on monolayer graphene by chemical vapor deposition (CVD). **Figure 4**a shows the schematic of the realized phototransistor device. The responsivity and the photocurrent response of the device are presented in Figure 4b. To improve the dark current due to lack of intrinsic gap in graphene, the authors in[78] exploited pulsed laser deposition (PLD)-grown Bi_2Te_3 (100 nm thick) on n-Si to achieve the rectification ratio exceeding 5×10^3. Vertically constructed PD exhibited photodetection from the ultraviolet (370.6 nm) to terahertz (118 μm) at room temperature. A summary of the characterization of the performance of the device is provided in **Table 2**. Development of heterostructure PDs based on TMs with abrupt junction is a very important step to realize

Table 2. TMs-based PDs. The units of D^* are in Jones; 1 Jones = (cm Hz$^{1/2}$ W^{-1}), G: photoconductive gain, TDS: topological Dirac semimetal, WS: Weyl semimetal, TCI: topological crystalline insulator, OOR: current on/off ratio, response time or rise time τ_{on}, τ_{on}/τ_{off}, [in ms]).

Material	Responsivity	D^*	Spectral response	G	OOR	τ_{on} / τ_{off}	Phase	Year	Ref.
Bi$_2$Te$_3$/graphene	35 AW^{-1} (@532 nm)	–	400–1550 nm	83	–	8.7/14.8	TI	2015	[47]
Bi$_2$Te$_3$/Si	1 AW^{-1} (@635 nm)	2.5×10^{11}	370–118000 nm	–	–	100/100	TI	2015	[78]
Sb$_2$Te$_3$	21.7 AW^{-1} (@980 nm)	1.22×10^{11}	980	27.4	2.36	$238 \times 10^3/203 \times 10^3$	TI	2015	[48]
Bi$_2$Se$_3$/Si	24.28 AW^{-1} (@808 nm)	4.39×10^{12}	300–1100 nm	37.4	1.55×10^5	2.5/5.5	TI	2016	[79]
SnTe	3.75 AW^{-1} (@2003 nm)	–	405–3800 nm	–	–	0.31/0.85	TCI	2016	[83]
WS$_2$/Bi$_2$Te$_3$	30.7 AW^{-1} (@1550 nm)	2.3×10^{11}	370–1550 nm	–	–	20/20	TI	2016	[49]
Cd$_3$As$_2$	2.0 mAW^{-1} (@633 nm)	–	370–1550 nm	–	–	6.9×10^{-6}/–	TDS	2017	[50]
Bi$_2$Te$_3$/SnSe/Bi$_2$Te$_3$	5.5 AW^{-1} (@370 nm)	6×10^{10}	370–808 nm	18.3	–	40/60	TI	2017	[84]
SnTe/Si	2.36 AW^{-1} (@1064 nm)	1.54×10^{14}	1064 nm	–	8×10^6	$2.2 \times 10^{-3}/3.8 \times 10^{-3}$	TCI	2017	[80]
Cd$_3$As$_2$/pentacene	36.15 mAW^{-1} (@650 nm)	–	450–10 600 nm	–	–	34/63	TDS	2018	[62]
TaAs	0.7 mAW^{-1} (@438 nm)	1.67×10^8	438–10 200 nm	–	–	–	WS/type I	2018	[60]
MoTe$_2$	0.40 mAW^{-1} (@532 nm)	1.07×10^8	532–10 600 nm	–	–	43×10^3/–	WS/type II	2018	[85]
Bi$_2$Se$_3$	23.8 AW^{-1} (@1465 nm)	8.0×10^{10}	1465 nm	20.3	972.5	540/420	TI	2018	[51]
SnTe	71.11 AW^{-1} (@254 nm)	–	254–4650 nm	–	–	0.21/0.73	TCI	2018	[61]
TaIrTe$_4$	20 µAW^{-1} (@10.6 µm)	1.4×10^6	532–10 600 nm	–	–	27×10^3/–	WS/type II	2018	[86]
Bi$_2$Te$_3$/pentacene	14.89 AW^{-1} (@650 nm)	7.8×10^{10}	450–3500 nm	28.4	–	1.89/2.47	TI	2019	[87]
Cd$_3$As$_2$/organic	729 mAW^{-1} (@808 nm)	–	365–10 600 nm	11.2	6268	$282 \times 10^{-3}/517 \times 10^{-3}$	TDS	2019	[88]
WS$_2$/Bi$_2$Te$_3$	20.5 AW^{-1} (@633 nm)	–	375–1550 nm	–	1.8×10^4	$180 \times 10^{-3}/517 \times 10^{-3}$	TI	2019	[89]
WTe$_2$	250 AW^{-1} (@3.8 µm)	–	514–10 600 nm	–	–	–	WS/type II	2019	[90]
TaAs	0.7 mAW^{-1} (@10.6 µm)	–	400–14 000 nm	–	–	200/–	WS/type I	2019	[91]
SnTe/Bi$_2$Se$_3$	145.74 mAW^{-1} (@1550 nm)	1.15×10^{10}	1550 nm	–	6.52	$6.9 \times 10^{-3}/19.2 \times 10^{-3}$	TCI/TI	2020	[92]
Bi$_2$Se$_3$/MoO$_3$	1.6×10^4 AW^{-1} (@ 405 nm)	5.79×10^{11}	405–1550 nm	4900	5.32×10^4	$63 \times 10^{-3}/73 \times 10^{-3}$	TI	2020	[64]
PtTe$_2$	40 AW^{-1} (@ 633 nm)	–	532–4000 nm	–	–	34×10^{-3}/–	TDS	2020	[93]
Sb$_2$Se$_3$	4320 mAW^{-1} (@532 nm)	–	300–1000 nm	10	17	13.16/9.61	TI	2020	[94]
(Cd$_{1-x}$Zn$_x$)$_3$As$_2$/MoO$_3$	3.1 AW^{-1} (@650 nm)	6.42×10^{10}	405–4500 nm	8.55	–	30/280	TDS	2020	[95]
Bi$_2$Se$_3$	168.9 mAW^{-1} (@900 nm)	1.85×10^{11}	200–1200 nm	–	113	4/–	TI	2020	[96]
Bi$_2$Se$_3$/graphite	26.69 µAW^{-1} (@1064 nm)	–	1064 nm	–	–	–	TI	2020	[63]
Sb$_2$Te$_3$/Si	270 AW^{-1} (@2400 nm)	1.28×10^{13}	250–2400 nm	–	–	129/132.2	TI	2020	[97]
Cd$_3$As$_2$/CuPc	142.5 AW^{-1} (@808 nm)	7.83×10^{10}	808–980 nm	–	–	–	TDS	2021	[98]

functional devices. (See Appendix 1 for a summary of the state-of-the-art synthesis methods for TMs).

It has been shown that the cost and the quality of deposition can be further improved by exploiting physical vapor deposition (PVD) method. In ref. [79], Zhang et al. used PVD to realize Bi$_2$Se$_3$/Si heterostructure with an atomically abrupt interface (Figure 4c). Photogenerated electron-hole in this case is separated via the built-in field at the junction. The PD exhibits detectivity as high as 4.39×10^{12} Jones and responsivity of 24.28 AW^{-1} at 808 nm. Zheng et al.[48] reported that single crystal SbTe grown with MBE can further improve sensitivity to the near-infrared light. The responsivity and photoconductive gain were estimated to be 21.7 A W^{-1} and 27.4, respectively. Schematic of the structure is shown in Figure 4d.

Surface states of TCIs and physical properties such as magnetism, superconductivity that are tunable via applying external strain or electrical field can be exploited to realize efficient photodetection in the near and mid-infrared range.[61,80–83] The pioneering work was done by Jiang and his colleagues

using SnTe.[83] In this work, high quality SnTe film was grown using MBE on strontium titanate (STO) with four quintuple layers (4 nm) of Bi$_2$Te$_3$ buffer. Compared to more common substrates such as Silicon and SiO$_2$, STO has a closer lattice constant to SnTe which allows high-quality growth. The fabricated photoconductive detector demonstrated efficient, fast, and stable response. The photoresponse measurements of the large-scale films from the visible (405 nm) to the mid-infrared range (3.8 µm) revealed high responsivity detection at room temperature.

A critical achievement in using TMs in PDs was the first demonstration of a TDS based PD.[50] TDSs as analogs of graphene have larger absorption due to bulk 3D structure. Another advantageous of TDSs is that the photoresponse spectrum has less fluctuations due to lack of a bandgap. The work by Wang and colleagues uses a metal-Cd$_3$As$_2$-metal PD structure to assess the electro-optical characteristics of the device. Schematics of the CVD synthesized Cd$_3$As$_2$ nanowires and nanoplates are shown in Figure 4e. Nanowire device channel is between 7 to 8 µm
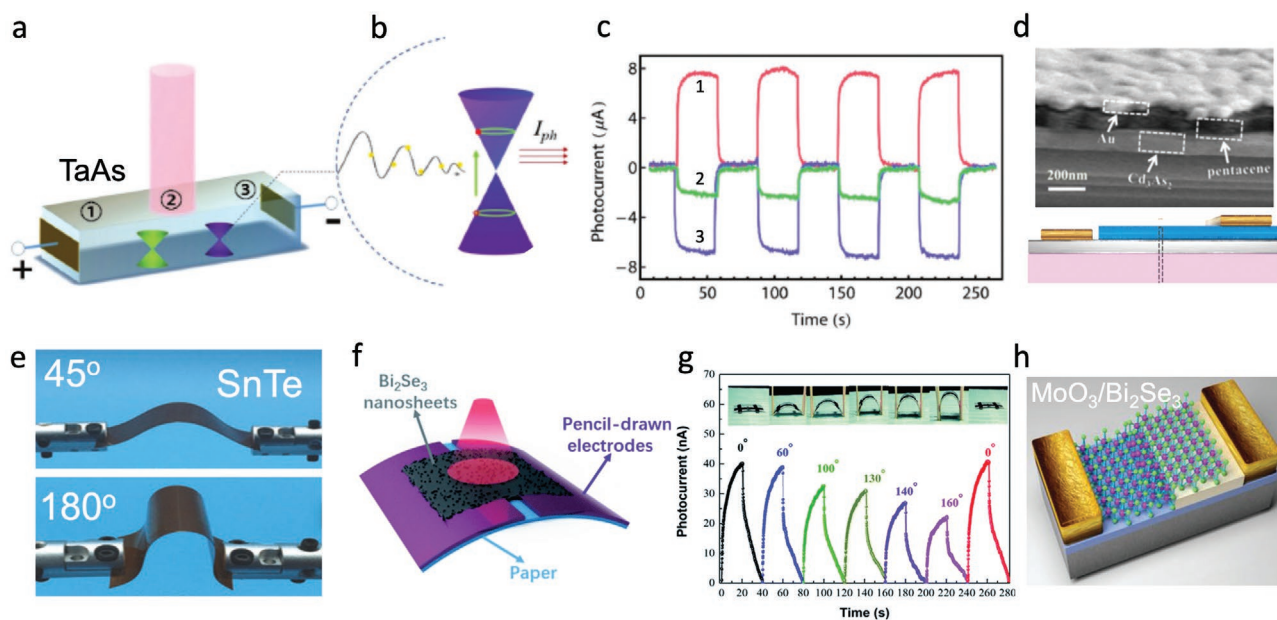
Figure 5. a) A schematic of the experimental setup for photoresponse analysis of TaAs PD. Labeled spots show the laser excitation locations. b) Photocurrent (I_{ph}) generation process in Weyl semimetals with linear dispersion. c) Time-resolved results of the position-dependent photoresponse in TaAs for the spots numbered in (a). Reproduced with permission.[60] Copyright 2017, Wiley-VCH. d) Schematic and SEM images of the Cd_3As_2 PD structure on pentacene. Reproduced with permission.[62] Copyright 2018, American Chemical Society. e) A TCI-based (SnTe) PD on an organic PET substrate under two different bending angles. Reproduced with permission.[61] Copyright 2018, Wiley-VCH. f) Schematic showing a bendable Bi_2Se_3 PD on a paper. g) Corresponding photocurrent of the PD in (f) under different bending angles. Reproduced with permission.[63] Copyright 2020, Royal Society of Chemistry. h) Bi_2Se_3/MoO_3 heterojunction PD. Reproduced with permission.[64] Copyright 2020, Wiley-VCH.

with the diameter varing from 100 to 200 nm. The nanoplates have a channel length of 5–15 µm and are about 200 nm thick. Analysis of the spatially resolved scanning photocurrent microscopy shows that the photocurrent distribution of the nanowire device is along the wire while the photoresponse of the nanoplate device is mainly at the Cd_3As_2-metal contact interface. Both PD structures show an ultrafast photocurrent response (6.87 ps) as illustrated in Figure 4f. Additional photodetecting characteristics of the device are summarized in Table 2.

PDs for infrared light detection at optical communications (1300–1650 nm) are extremely important for present telecommunication infrastructure. Layered Bi_2Se_3 as a TI was demonstrated to be a promising candidate for infrared detectors. Wang et al. have reported an ultrathin PD at 1456 nm in the E-band of the communication range based on 2D Bi_2Se_3 flakes.[51] Submillimeter sized Bi_2Se_3 flakes grown on mica substrate using van der Waals epitaxy method with atomic resolution. The realized back-gated FET device structure is schematically drawn in Figure 4g. It was found that the geometrical properties of the Bi_2Se_3 flakes can be tuned by adjusting the growth temperature. Fabricated PD based on Bi_2Se_3 flake exhibits an ultrahigh on/off current ratio of 972.5 at 1456 nm. Furthermore, the time-resolved analysis demonstrated a very high responsivity of 23.8 AW^{-1} and D^* of 8.0×10^{10}, respectively (see Figure 4h). The realization of millimeter size layered TI flakes in this work motivate the exploration and fabrication of other 2D TI materials.

To expand the detection range further, mid- and even long-infrared, authors in ref. [60] have exploited prototype Weyl semimetal TaAs. TaAs with a linear energy–momentum relation hosts chiral massless Weyl Fermions and is demonstrated to have an ultra-broadband photoresponse at room

temperature.[91,99] In addition, TaAs, like other Weyl semimetals, exhibits features such as high carrier mobility, reduced lattice thermal conductivity, and helicity-dependent photocurrent that are critical for the improvement of present PDs. **Figure 5**a shows the photocurrent measurement setup on a slab of single crystal TaAs with 2 mm × 2 mm footprint and 1.1 mm thickness which is contacted using Cu electrodes. Both continuous wave and pulsed laser sources ranging from 438 nm up to 10.2 µm were used to study the broadband response of the device. Numbers 1, 2, 3 indicate the normal laser excitation spots on the sample. A schematic of the photocurrent generation principle in Weyl semimetals through interband transition of the Pauli blocking edge is illustrated in Figure 5b. The as-grown TaAs prototype exhibited a responsivity of 0.7 mA W^{-1} and a detectivity of 1.67×10^8 Jones at room temperature at 438 nm. The time-resolved measurements on the sample, shown in Figure 5c, indicate a position-dependent photocurrent response which is associated to the observed photothermoelectric effect.

TMs can also be integrated with organic materials. Compared to inorganic materials, organic polymers are cheap, solution processable, more accessible and less toxic (thus less concerning for biomedical applications)[62,88] Heterojunction of Cd_3As_2 (a prototype TDS) with pentacene is reported to have a broadband photoresponse from 450 nm to 10.6 µm at room temperature.[62] Acquired responsivity values were 36.15 and 1.55 mAW^{-1} at 650 nm and 10.6 µm, respectively. Compared to previous reports which mostly use nano-size crystal Cd_3As_2, Cd_3As_2 films present faster response time as a result of better relaxation time. An SEM image of the cross-section of the device is shown in Figure 5d. Each layer of the heterostructure is about

**ADVANCED
SCIENCE NEWS**
www.advancedsciencenews.com

**ADVANCED
FUNCTIONAL
MATERIALS**
www.afm-journal.de

100 nm thick. Besides having outstanding electrical, optical, and thermal properties, TMs can be integrated to achieve flexible PDs for a wide-range of applications. Authors in ref. [61] have used SnTe, a prototype TCI, with ultra-broad spectral response (254–4650 nm) to demonstrate a stable and flexible PD. The responsivity of the device can reach up to 71.11 AW^{-1} at 254 nm and 4.17 AW^{-1} at 4650 nm, respectively. Such a high responsivity is determined to be associated to the suppressed recombination of the photoexcited holes as a result of p-type charge carriers in SnTe. The fabricated PD on a organic polyethylene terephthalate (PET) substrate was shown to tolerate large bending angles by stable photocurrent as shown in Figure 5e.

Novel fabrication techniques can be integrated with TMs to reduce the production cost, improve efficiency and help integrating with other functional components. Pencil-drawing of liquid exfoliated Bi$_2$Se$_3$ nanosheets has been reported recently.[63] (Figure 5f) The electrodes were drawn using a graphite pencil on a paper. The realized flexible PD holds high infrared response with 0.35 μA photocurrent under the 3.76 mW mm^{-2} excitation at 1064 nm. As shown in Figure 5g, the device can withstand large bending angles up to 160° which is crucial for wearable applications.

Interfacing nanostructured TMs with atomically thin 2D materials is another interesting research direction that has been gaining interests in recent years. 2D materials permit tunable bandgap depending on the number of the layers along with convenient van der Waals integration with countless materials. Although breakthrough 2D PDs have been realized recently, most devices suffer from extremely narrow spectral response as well as low detection performance. Integration of TMs with transition metal chalcogenides can open up a plethora of applications in PDs. Tungsten disulfide (WS$_2$)/Bi$_2$Te$_3$ heterostructure has been demonstrated to create efficient carrier separation at the WS$_2$/Bi$_2$Te$_3$ heterointerface and remarkable transport properties along the time-reversal-symmetry protected surface of Bi$_2$Te$_3$.[89] The authors have reported high sensitivity to both visible and near infrared light illumination. The responsivity and detectivity were estimated to be 30.7 AW^{-1} and 2.3 × 10^{11} at 1550 nm. In,[100] Zhang et al. report a TDS (Cd$_3$As$_2$ nanobelt) on WS$_2$ heterojunction PD. The device was realized by placing mechanically exfoliated few-layer WS$_2$ on CVD grown Cd$_3$As$_2$ nano-belt. Exploiting strong light-matter interaction in TDSs, a large responsivity of 223.5 AW^{-1}, a detectivity of 2.1×10^{14} Jones, and a rapid response time of about 15 ms were obtained. The fabricated devices achieved a wide spectral response from visible (405 nm) to near-IR region (808 nm) at room-temperature.

Utilizing a similar concept, a high photoconductive gain graphene PD was fabricated using Bi$_2$Te$_3$ nanowire.[101] In this work, the low bandgap of Bi$_2$Te$_3$ increased photoresponsivity by about 200% as a result of the increased light absorption.

PDs based on TMs are presently under active improvement. Recent papers show fabricated devices with extremely high responsivity and ultra-broadband response.[64,95,97] Very recently Yang et al. have reported a device based on 3D TI Bi$_2$Se$_3$/MoO$_3$ with responsivity as high as 1.6 × 10^4 and 2.61 × 10^3 AW^{-1} at 405 and 1310 nm, respectively (Figure 5h). Recent advances in using TMs such as Bi$_2$Te$_2$Se for optical chirality detection[102]

and type-II TDS PtTe$_2$ for angle-sensitive detection[103] are promising to open up new directions in this field.

5. Nanophotonic and Plasmonic Devices

5.1. Nanostructures: Nanolayers, Nanosheets, Nanoplates, and Nanowires

Nanophotonic devices harnessing the outstanding optoelectronic properties of TIs, Dirac, and Weyl semimetals, have been mostly developed so far using binary, ternary and quaternary Bi and Sb chalcogenides as material platforms. Among the wide (Bi, Sb, Te, Se) compositional space, several compounds are 3D TIs. Such compounds consist of a small bandgap semi-conductor bulk and a highly conductive surface where conductivity is ensured by charge carriers in topological surface states enabling the propagation of spin-polarized currents, possibly together with a significant contribution of charge carriers in quantum well states appearing near the surface due to band bending or defects.[32] The bulk may also present a significant conductivity due to free charge carriers introduced by doping. The optoelectronic properties of both the bulk and surface are tunable in a static way by controlling the chalcogenide composition or by shaping the material into nanostructures with well-suited dimensions, and in a dynamic and reversible way through external solicitations such as a gate voltage, a mechanical deformation, or light pulses. These remarkable features are the cornerstone for the demonstration of passive, active or spin- nanophotonic devices with outstanding performance in a broad spectral range. Proof-of-concept devices have been demonstrated using nanostructures with a simple morphology, such as nanolayers, nanosheets, nanoplates, and nanowires.

5.1.1. Passive Nanophotonic Devices

Peng et al. reported infrared transparent electrodes based on Bi$_2$Se$_3$ nanosheets.[104] These electrodes combine a good conductance with a high transparency in the near infrared, where no sizeable over-bandgap and Drude optical absorption occur. This contrasts with ITO electrodes which are opaque in the infrared. This application may take a special profit from the high tunability of the optoelectronic properties of Bi and Sb chalcogenide nanosheets upon varying their thickness. Such tunability has been exemplified by Hussain et al., who reported a thickness-dependent bandgap and strong and tunable room-temperature photoluminescence in Bi$_2$Te$_3$ nanosheets.[105]

5.1.2. Active Nanophotonic Devices

In addition to static tuning by design and composition, the optoelectronic response of Bi and Sb chalcogenides can be tuned over a broad spectral range in a dynamic and reversible way through external solicitations. This is appealing for the fabrication of broadband active nanophotonic devices. Liu et al. tuned dynamically the optical transmittance and reflectance of
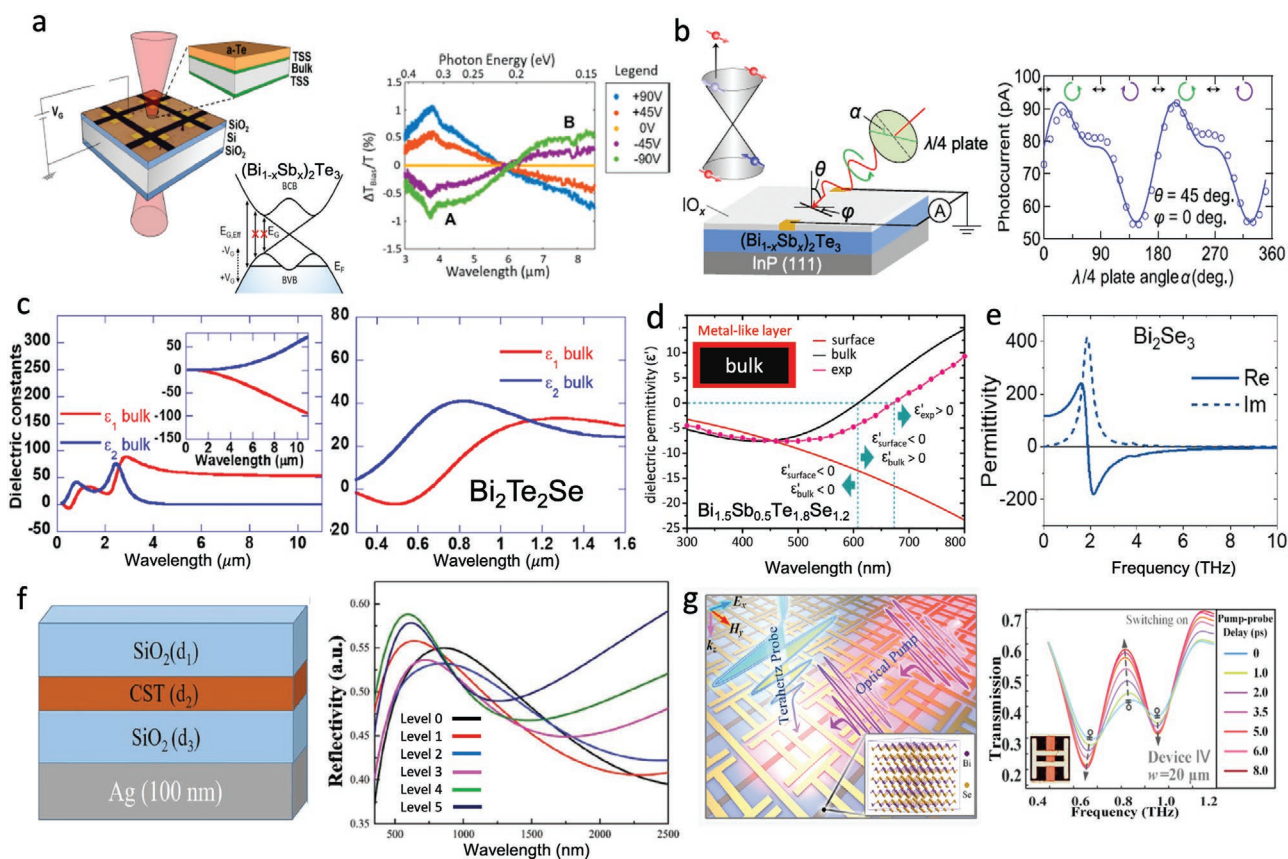
Figure 6. Nanophotonic devices based on TMs. a) Active broadband $(Bi_{1-x}Sb_x)_2Te_3$ nanolayer—based nanophotonic device with dynamically tunable transmittance upon application of a gate voltage. Schematic representation, performance, and tuning mechanism. Reproduced with permission.[108] Copyright 2017, American Chemical Society. b) Helicity-dependent photocurrent in $(Bi_{1-x}Sbx)_2Te_3$ nanolayers: observation and underlying mechanism. Reproduced with permission.[117] Copyright 2016, American Physical Society. c) Typical broadband bulk dielectric function in the ultraviolet, visible, and infrared regions of a chalcogenide TI (Bi_2Te_2Se). The surface dielectric function is also shown in the inset. Reproduced with permission.[118] Copyright 2019, American Chemical Society. d) Bulk and surface dielectric functions of $Bi_{1.5}Sb_{0.5}Te_{1.8}Se_{1.2}$ in the ultraviolet, visible, and near infrared regions. Reproduced with permission.[119] Copyright 2017, Wiley-VCH. e) Bulk dielectric function of Bi_2Se_3 in the THz region: evidence of a phonon mode. Reproduced with permission.[120] Copyright 2020, American Physical Society. f) Structure of a colorful metasurface built from a Sb_2Te_3-based nanolayer, and evolution of its reflectance spectrum upon irradiation with light pulses. Reproduced with permission.[121] Copyright 2018, Wiley-VCH. g) Metasurface based on Bi_2Se_3 ribbons for the ultrafast dynamic tuning of THz waves. Schematic representation and performance. Reproduced with permission.[122] Copyright 2021, American Chemical Society.

heavily n-doped Bi_2Se_3 nanoplates from the visible to the mid-infrared upon application of a gate voltage.[106]

Under a gate voltage with the chosen polarity, electrons are injected to or depleted from the bulk conduction band. This leads to enhancing or decreasing the corresponding Drude contribution in the mid infrared, respectively. This change in the band filling also modifies the over-bandgap optical transition probabilities in the nanoplates, and therefore the corresponding interband contribution in the visible to short wave infrared.[106,107] Based on a comparable mechanism yet involving topological surface states in addition to bulk electronic bands, Whitney et al. tuned dynamically the optical transmittance of a $(Bi_{1-x}Sb_x)_2Te_3$ nanolayer at longer wavelengths in the mid-infrared (**Figure 6**a).[108] These two types of bulk and surface channels were also involved in the dynamic electrical tuning of Bi_2Se_3 nanolayers reported by Jeon et al.[107] Park et al. reported the dynamic tuning of the Fermi level of Sb_2Te_3 nanolayers by mechanical deformation, which impacted their optical response in the visible range.[109]

The dynamic tuning of the optical properties of Bi and Sb chalcogenide nanostructures has also been thoroughly reported upon irradiation with ultrafast laser pulses.[110–116] Irradiation with visible/near infrared femtosecond light pulses was shown to induce an ultrafast nonlinear optical response at visible/near infrared frequencies in the nanostructures. This response is appealing for devices such as all-optical switches or saturable absorbers.[110,111] Irradiation with visible/near infrared femtosecond light pulses was also shown to enable the ultrafast dynamic tuning of the THz properties of the nanostructures.[112–116] Their THz properties were shown to evolve on a time scale ranging from a few picoseconds to few hundreds of picoseconds after the pulse. Such temporal behavior and the underlying electronic mechanism depend on several variables, such as the nanostructure composition, crystal structure, dimensions, temperature, and position of the Fermi level. For example, Shi et al. studied the time-dependent room-temperature THz response of Bi_2Se_3 nanolayers with their Fermi level located in the bulk bandgap.[115] To interpret the observed response, they proposed that the near infrared pump first excites electrons from the bulk valence band to the bulk conduction band, and that the photoexcited carriers then scatter into topological surface states.[115]

**ADVANCED
SCIENCE NEWS**
www.advancedsciencenews.com

**ADVANCED
FUNCTIONAL
MATERIALS**
www.afm-journal.de

Box 2: Plasmons in TIs Versus Plasmons in Metals

Plasmons and plasmon resonances are observed in both noble metals and TIs. While presenting some similarities, such as field confinement or a marked spectral tunability upon design of nanostructures of suitable morphology, plasmons, and plasmon resonances in these two classes of materials have very different physical origins. This leads to some very different properties. Plasmon resonances in noble metals originate from the excitation of Drude carriers in the bulk conduction band, and then decay either radiatively or nonradiatively (for instance by scattering at defects or through interband transitions). Plasmon resonances in TIs originate from very different paths, such as the excitation of bulk interband transitions (ultraviolet–visible plasmons) or of charge carriers in topological surface states in a nanometric layer near the material surface (plasmons in the infrared/THz, possibly up to the visible–near infrared). Ultraviolet–visible interband-induced plasmon resonances in TIs can be made broader than the resonances in noble metals and thus be more suitable for efficient light harvesting. In contrast with noble metals, plasmon resonances in TIs have a broad potential for being tuned dynamically, for instance by phase transitions, by electrical gating, with a magnetic field or with light. This is appealing for achieving active nanophotonic devices operating in the ultraviolet–visible, infrared or THz. Furthermore, thanks to the spin–momentum locking of charge carriers in topological surface states and their insensitivity to defects, TIs are appealing for low-loss and spin-plasmonic applications.

Park et al. studied the time-dependent room-temperature THz response of single-crystal Bi_2Te_3 nanowires.[116] To account for the observed response, they proposed that it involves electronic transitions between bulk electronic bands, topological surface states, and quantum well states. An interplay between optically-excited bulk electronic bands and topological surface states is appealing for many reasons. First, it enables harnessing the efficient absorption of visible or near infrared light by the bulk to dynamically tune THz properties in a practical way. Second, it is relevant for the design of PDs combining an efficient harvesting of visible and near infrared light by absorbing bulk channels, with an efficient extraction of photogenerated carriers through high-mobility topological surface channels. And last, but not least, the suitable control of the interplay between bulk channels and topological surface channels opens the way to efficient spin-nanophotonic devices.

5.1.3. Spin-Nanophotonic Devices

In $(Bi_{1-x}Sb_x)_2Te_3$ nanolayers, the interaction of circularly polarized light with spin-polarized surface currents has been shown to lead to the generation of helicity-dependent photocurrents (Figure 6b).[117,123] This effect is appealing for the design of chirality-sensitive PDs. It was observed with near infrared light, which triggers the photoexcitation of electrons between surface and bulk energy bands. Properly setting the Fermi level is needed to optimize electron transfers between these energy bands, and thus the helicity-dependent photocurrent.

5.2. Nanostructured Metamaterials Harnessing Optically Metallic, Plasmonic, Epsilon-Near-Zero, and Ultrahigh Refractive Index Properties

In relation with their outstanding optoelectronic properties that involve surface and bulk charge carriers, Bi and Sb chalcogenide TIs present a different dielectric character in their volume and in a nanometric layer at their surface.[118,124,125] The corresponding bulk and surface dielectric functions ($\varepsilon^{bulk} = \varepsilon_1^{bulk} + i\varepsilon_2^{bulk}$ and $\varepsilon^{surface} = \varepsilon_1^{surface} + i\varepsilon_2^{surface}$) display unconventional spectral features. These features endow Bi and Sb chalcogenides with optically metallic, plasmonic, epsilon-near-zero and ultrahigh refractive index properties in different spectral regions. This makes these compounds excellent candidates for the design of nanostructured metamaterials enabling ultracompact nanophotonic devices for a wide gamut of applications in a wide spectral range.

5.2.1. Bulk and Surface Dielectric Functions of Bi and Sb Chalcogenides

The bulk dielectric functions of Bi and Sb chalcogenides are dominated by intense interband transitions peaking at wavelengths smaller than the bandgap threshold wavelength.[130,132,133] These interband transitions induce a negative bulk dielectric permittivity ($\varepsilon_1^{bulk} < 0$) at shorter wavelengths (usually, across the ultraviolet–visible), a canceling bulk dielectric permittivity ($\varepsilon_1^{bulk} = 0$ at two specific wavelengths (usually, in the ultraviolet-visible), and an optically dielectric response ($\varepsilon_1^{bulk} > 0$) with an ultrahigh bulk refractive index at longer wavelengths (usually, in the infrared) (Figure 6c).[125,130,132,133] These well contrasted spectral features, which are inherited from those of Bi, Sb, Te, and Se,[133–135] make Bi and Sb chalcogenides suitable for displaying optically metallic, plasmonic and epsilon-near-zero properties in the ultraviolet–visible and ultrahigh refractive index properties in the infrared. The exact spectral region and the features accessible to these properties are tunable by controlling the chalcogenide composition.[130,132,133,136–139] The ultraviolet–visible bulk dielectric functions of Bi and Sb chalcogenides are prone to enabling a strong optical confinement in deeply subwavelength nanoscale volumes. However, they feature stronger losses (higher ε_2^{bulk}) than those of noble metals, Ag and Au. Therefore, these compounds are better suited for applications affording or requiring broader spectral features, smaller plasmon propagation lengths and near-field enhancements than those enabled by these metals.[132,133,136] Their infrared bulk refractive index reaches values up to 10, way superior to that of usual semiconductors such as Si and Ge.[130,133] Therefore, they present an unrivaled potential for applications requiring the deeply subwavelength

ADVANCED
SCIENCE NEWS
www.advancedsciencenews.com

ADVANCED
FUNCTIONAL
MATERIALS
www.afm-journal.de

nanoscale manipulation of infrared light on optically dielectric material platforms. Besides these interband-induced properties, negative, and canceling values of the bulk dielectric permittivity (and thus optically metallic, plasmonic and epsilon-near-zero properties) can also be induced in the infrared and/or THz by bulk free charge carriers if the material is suitably doped. Furthermore, it has been proposed that surface charge carriers occupying topological or quantum well states induce a negative surface permittivity ($\varepsilon_1^{surface} < 0$).[118,124,125,132] Although typically expected in the infrared/THz region, negative surface permittivity has been reported up to the visible (Figure 6d).[124,125,132] When dominated by the contribution of topological states, this negative surface permittivity is appealing for low loss plasmonic applications. To develop such applications, it is needed to minimize bulk optical losses, for instance by using ultrathin nanolayer platforms or by operating in a spectral region where $\varepsilon_1^{surface} < 0$ and ε_2^{bulk} is small, for example, in the infrared. Other applications have been proposed that would harness the interaction between surface and bulk dielectric properties to achieve hybrid optical modes. For example, the interaction between charge carriers at topological surface states and bulk phonon modes peaking in the THz (Figure 6e) is appealing to achieve dynamically tunable hybrid topological plasmon–phonon modes in the THz spectral region.[32]

5.2.2. Nanophotonic Devices Harnessing Optically Metallic Properties

The optically metallic response of Bi and Sb chalcogenides in the ultraviolet–visible and infrared/THz is attractive for the design of metamaterial-based ultracompact nanophotonic devices. Meng et al. reported colorful metasurfaces built from Sb_2Te_3-based nanolayers (Figure 6f).[121] The colorful aspect of these metasurfaces is enabled by optical interference harnessing the semi-transparent character of the Sb_2Te_3-based nanolayers in the visible. The structural color of these metasurfaces can be tuned accurately by triggering phase transitions with light pulses. This is appealing for ultrathin display applications. Yue et al. reported that optical interference in Sb_2Te_3 nanolayers enables strong and thickness-sensitive phase shifts for the reflected visible light.[140] This effect was attributed to the markedly different dielectric functions of the surface and bulk of the nanolayers, which behave as intrinsic optical cavities. It was applied for the design of metasurfaces acting as ultrathin hologram formation devices. Metasurfaces can also harness the natural optical anisotropy of Bi and Sb chalcogenides. By characterizing the usually unreported optical properties of Bi_2Se_3 and Bi_2Te_3 along their optical axis, Esslinger et al. demonstrated that these compounds display optical hyperbolism in the near infrared to visible.[141] They obtained positive values of the bulk dielectric permittivity along this axis, in contrast with the negative values of the usually reported ordinary bulk dielectric permittivity. This can be applied for the design of ultrathin superlenses for near-field microscopy and sharp far-field isoindex filters. Hu et al. harnessed the optically metallic THz response of Bi_2Se_3 and its tunability under external solicitations to fabricate metasurfaces enabling an efficient modulation of THz light waves (Figure 6g).[122] In these metasurfaces,

ultrathin Bi_2Se_3 ribbons are used to electromagnetically shunt metal antennas in a dynamic way. By shining femtosecond near infrared light pulses on the Bi_2Se_3 ribbons, their bulk and surface charge carrier densities, and thus their THz dielectric function change. This enables tuning, on the timescale of few picoseconds, the THz optical transmittance of the metasurface. This can be applied to develop all-optical ultrathin THz switches.

5.2.3. Nanophotonic Devices Harnessing Plasmonic Properties

Ultraviolet-visible plasmonic properties have been demonstrated in different types of Bi and Sb chalcogenide nanostructures: Bi_2Te_2Se nanoflakes,[118] Bi_2Te_3 nanoplates,[126,142] $Bi_{1.5}Sb_{0.5}Te_{1.8}Se_{1.2}$ nanodisks, and nanoflakes,[119] Bi_2Te_3 nanoflakes with bullseye surface structures,[143] Bi_2Se_3 nanoflowers,[144] arrays of nanoslits and nanogratings in $Bi_{1.5}Sb_{0.5}Te_{1.8}Se_{1.2}$,[124] arrays of nanogratings in Bi(34%):Te(66%),[136] arrays of nanogratings in Sb_2Te_3,[145] arrays of nanocones in $Bi_{1.5}Sb_{0.5}Te_{1.8}Se_{1.2}$,[125] Sb_2Te_3 nanolayers.[146] Dyakonov plasmons and edge polaritons have also been reported in Bi_2Se_3 nanoplates.[147,148] In most cases, the plasmonic properties seem to be related mostly with the interband-induced negative bulk permittivity values ($\varepsilon_1^{bulk} < 0$) of the considered chalcogenide in the ultraviolet–visible, although in some cases the surface dielectric permittivity was proposed to play a significant role.[124] The spectral features of the plasmon resonances reported in such nanostructures were shown to be tunable by design. As observed for conventional plasmonic materials such as Ag and Au, the plasmon resonance wavelength and spectral width can be tuned by controlling the nanostructure size and shape,[124,125,145] organization,[125,136] and composition (**Figure 7**a).[126] The plasmon resonance wavelength and spectral width can also be tuned dynamically by triggering phase transitions in the chalcogenide material (Figure 7a).[126] The specific optical absorption, dispersion, and near-field enhancement induced by ultraviolet–visible plasmons in Bi and Sb chalcogenide nanostructures have enabled building metamaterial-based nanophotonic devices for several applications. The dependence of the plasmon resonance features on the nanostructure size, shape and organization has been harnessed by Ou et al.[124] and Piccinotti et al.[136] to tailor metamaterials displaying tunable and polarization-dependent structural colors. The particularly broad spectral width of plasmon resonances in Bi and Sb chalcogenide nanostructures is ideal for light harvesting, and this has enabled the fabrication of Bi_2Se_3 metamaterial-based broadband light absorbers for efficient photothermal conversion, as reported by Guozhi et al.[144] By coupling plasmons into suitably designed dispersive Sb_2Te_3 metasurfaces, Yue et al. produced optical angular-momentum detectors.[149] By harnessing the enhanced near field at the vicinity of Bi_2Te_3 nanoplate arrays, Zhao et al.[126] and Saleem et al.[142] reported the enhancement of quantum dot fluorescence. The performance of these different devices was apparently mostly driven by the interband-induced bulk dielectric properties of the chalcogenide. However, in a very recent work, Sun et al. have reported a $Bi_{1.5}Sb_{0.5}Te_{1.8}Se_{1.2}$ metamaterial where both the bulk and surface dielectric properties play an important role. In this metamaterial, visible plasmons
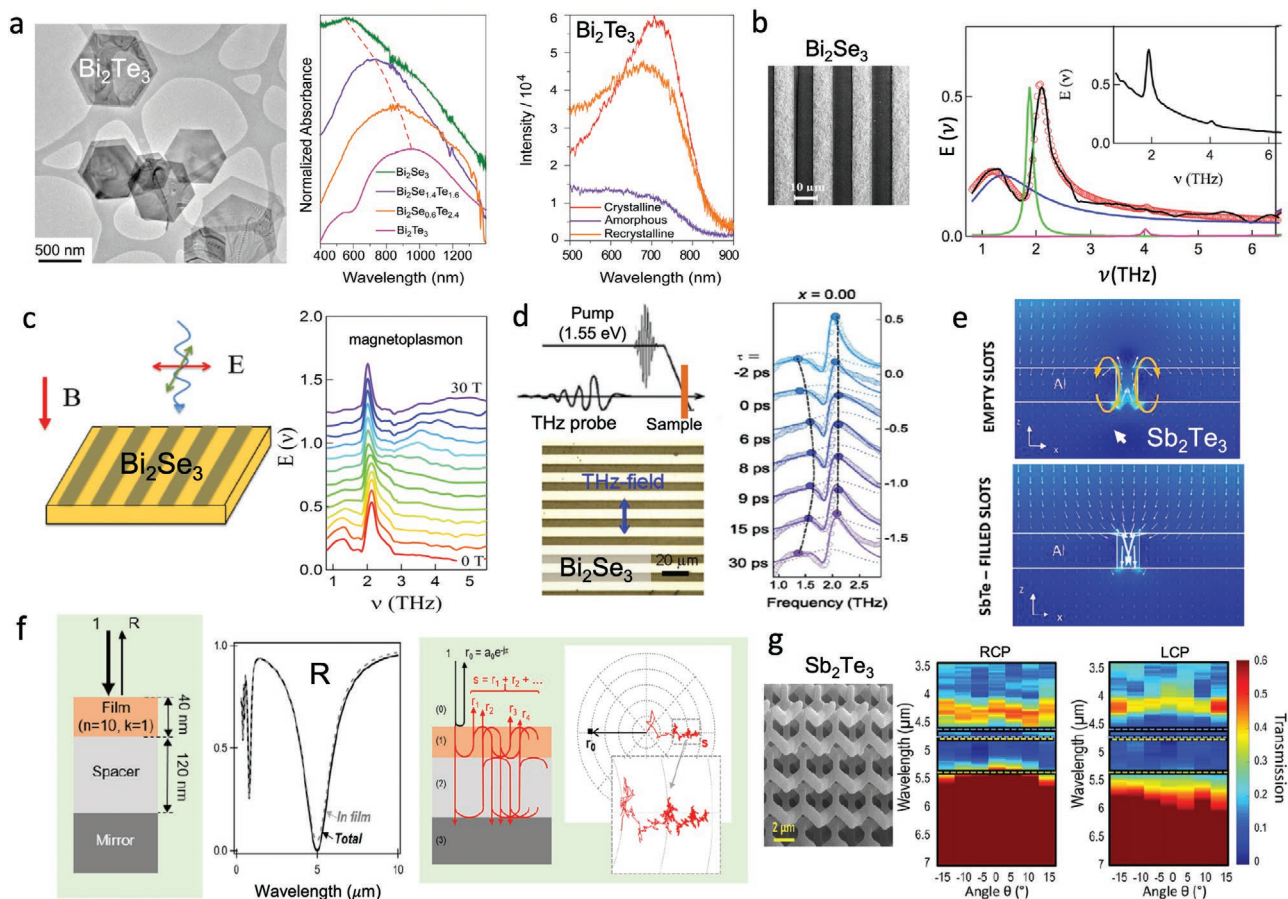
Figure 7. a) Ultraviolet visible plasmonics with chalcogenide nanoplates: structure, tuning with composition, and tuning upon phase transition. Reproduced with permission.[126] Copyright 2016, Wiley-VCH. b) THz plasmonics with a ribbon-structured nanolayered Bi_2Se_3 metamaterial: structure, optical response. The extinction spectrum (black and red lines) can be decomposed into several components: a plasmon resonance (blue line) and a phonon mode (green line). Reproduced with permission.[127] Copyright 2016, American Chemical Society. c) Dynamic tuning of the THz plasmonic response of a ribbon-structured nanolayered Bi_2Se_3 metamaterial with a magnetic field: scheme, and optical response. Reproduced with permission.[127] Copyright 2016, American Chemical Society. d) Ultrafast dynamic tuning of the THz plasmonic response of a ribbon-structured nanolayered Bi_2Se_3 metamaterial upon irradiation with near infrared light pulses: scheme, and optical response. Reproduced with permission.[128] Copyright 2015, American Chemical Society. e) Laminar flow through a nanohole filled with Sb_2Te_3, compared with the case of an empty nanohole. Reproduced with permission.[129] Copyright 2018, Wiley-VCH. f) Simple metasurface enabling the perfect absorption of infrared light in a $\lambda/100$ nanolayer with ultrahigh refractive index. Structure, performance, and fractal interference mechanism enabling the perfect absorption. Reproduced with permission.[130] Copyright 2018, Optica Publishing Group. g) Sb_2Te_3—based metamaterial with a chiral infrared photonic bandgap. Structure and performance (RCP = right-handed circular polarization, LCP = left-handed circular polarization). Reproduced with permission.[131] Copyright 2018, Wiley-VCH.

resulting from the interband-induced negative bulk permittivity of the material enhance the coupling between circularly polarized light and spin-polarized topological surface currents.[150] This mechanism is appealing for the development of ultrathin chirality-sensitive PDs with an optimal performance. Plasmonic properties have also been demonstrated in Bi and Sb chalcogenide nanostructures at infrared and THz frequencies. Such properties arise from a negative bulk dielectric permittivity ($\varepsilon_1^{bulk} < 0$, due to bulk free charge carriers) and/or from a negative surface dielectric permittivity ($\varepsilon_1^{surface} < 0$, due to charge carriers in topological surface states or in quantum well states). Far infrared plasmons propagating at the surface of Bi_2Te_2Se nanoflakes have been reported by Venuthurumilli et al.[118] Their wavelength was nearly 100 times smaller than the incident wavelength. This was attributed to the fact that such plasmons are induced by carriers in the surface states of the nanoflakes. THz plasmons have been thoroughly reported

in Bi chalcogenide metasurfaces, in the frequency range from 1 to 5 THz (Figure 7b). Di Pietro et al. observed THz plasmon resonances in ribbon-structured nanolayered Bi_2Se_3 metasurfaces.[151] By analyzing the dispersion law of such resonances, the authors stated that they are induced by charge carriers in topological surface states. Kogar et al. proposed that the observed resonances could be induced by bulk free carriers as well.[152] Ginley et al. also reported THz plasmons in ribbon-structured nanolayered Bi_2Se_3 metasurfaces, and they pointed out that they are coupled excitations involving charge carriers in topological surface states at the top and bottom interfaces of the nanolayers.[153] The frequency and width of the THz plasmon resonances reported in these works can be tuned by design, for example, by adjusting the ribbon width,[151,153] and nanolayer thickness.[153] When set at the suitable frequency, the THz plasmon resonance hybridizes with the narrow phonon mode of Bi_2Se_3 near 2 THz, thus leading to a Fano

**ADVANCED
SCIENCE NEWS**

www.advancedsciencenews.com

**ADVANCED
FUNCTIONAL
MATERIALS**

www.afm-journal.de

resonance (Figure 7b).[151,153] THz plasmons, Fano resonances, and spectral tunability have also been evidenced in other types of metasurfaces, for instance in ring-structured nanolayered Bi_2Se_3 metasurfaces as reported by Autore et al.,[154] or in slit-structured nanolayered Bi_2Se_3 metasurfaces as reported by In et al.[155] Furthermore, Wang et al. showed that a broader spectral tunability can be achieved upon designing the metasurfaces from a multilayer stack with tailored sequence and layer thicknesses instead of a single nanolayer.[120] This enables harnessing the coupling between different chalcogenide layers to achieve multiple resonances. The tuning of the THz Fano and plasmon resonance spectral features has also been reported by varying the chalcogenide composition. In particular, Autore et al. observed a broadening of the THz plasmon resonance upon In doping of nanolayered Bi_2Se_3 metasurfaces, which they attributed to the disappearance of topological surface states.[156] Dynamic tuning of the THz spectral features has also been reported in Bi chalcogenide metasurfaces and is particularly relevant for active THz devices. Autore et al. achieved the tuning of the THz plasmon resonance in nanolayered Bi_2Se_3 metasurfaces by applying an external magnetic field (Figure 7c).[128] Di Pietro et al. used high intensity pulsed synchrotron THz radiation to modulate the THz plasmon resonance of nanolayered Bi_2Se_3 metasurfaces.[157] Sim et al.[127,158] and Lu et al.[159] tuned dynamically the THz spectral response of nanolayered Bi_2Se_3 metasurfaces with near-infrared femtosecond laser pulses (Figure 7d). The THz properties were shown to evolve on a time scale of a few picoseconds after the pulse. A modulation depth of up to 2400% was achieved in the THz extinction spectrum for a low pulse fluence.[158] This was enabled by the THz Fano resonant character of the metasurface, which involves charge carriers in surface states together with bulk phonons, and by the strong bulk interband absorption of Bi_2Se_3 in the near infrared. This demonstrates the interest of Bi and Sb chalcogenides as material platforms combining surface and bulk phenomena for nanophotonic devices with outstanding properties.

5.2.4. Nanophotonic Devices Harnessing Epsilon-Near-Zero Properties

Piccinotti et al. reported that filling nanoholes in metal nanolayers with Sb_2Te_3 enables a laminar flow transmission of ultraviolet–visible light with an increased absorption and decreased Joule losses (Figure 7e).[129] This can find applications in nanophotonic devices for transmission enhancement, wavefront shaping and controlled spontaneous emission.

5.2.5. Nanophotonic Devices Harnessing Ultrahigh Refractive Index Properties

The outstanding optical properties enabled by the ultrahigh infrared refractive index of Bi and Sb chalcogenides are already apparent in a simple metasurface consisting of a nanolayer deposited on a spacer and mirror. If the nanolayer presents a small extinction coefficient together with its ultrahigh refractive index, the nanolayer/spacer/mirror structure behaves as a resonant optical cavity enabling perfect absorption of infrared light through a fractal interference mechanism (Figure 7f). This

enables such perfect absorption to occur in a nanolayer more than 100 times thinner than the wavelength.[130] The ultrahigh infrared refractive index of Bi and Sb chalcogenides is also an asset for nano-waveguiding applications, as reported by Chai et al. in the case of Bi_2Te_3.[160] The great potential of more complex chalcogenide metamaterial structures for the nanoscale manipulation of infrared light has also been demonstrated. Krishnamoorthy et al. fabricated infrared resonant Bi_2Te_3 – based nanoslit metamaterials showing complex mode structures with surface circular currents, bringing opportunities to couple light with spin-polarized topological surface carriers.[161] Goi et al. fabricated metamaterials based on polymer core—Sb_2Te_3 shell nano-gyroids for an application to infrared chiral nanophotonic devices (Figure 7g).[131] By combining the ultrahigh refractive index of Sb_2Te_3 with a bio-inspired polymer network, they achieved a photonic structure with a high effective index and a photonic bandgap sensitive to the circular polarization of the incident infrared light.

5.2.6. Other TMs for Nanophotonics and Plasmonics

Beyond Bi and Sb chalcogenides, other TMs belonging to the classes of TIs, TDSs, and Weyl semimetals are emerging as appealing building blocks for nanophotonic and plasmonic devices. Efforts are being made to unveil the optoelectronic properties of such materials and assess their relevance for devices. Some examples are given hereafter.

5.2.7. Cd_3As_2 (TDS)

Chorsi et al. demonstrated that the optical properties of Cd_3As_2 thin films in the mid and far infrared are strongly sensitive to temperature, because of the dynamic tuning of the Fermi level and a varying Drude response.[52] Jia et al. proposed to harness this temperature sensitivity to design metasurfaces for the active control of circularly polarized infrared light.[162] Dai et al. reported the ultrafast optical tuning of the THz response of Cd_3As_2 thin films. Such tuning was achieved by irradiation with near infrared femtosecond laser pulses.[163] The switching time was in the range of 10 ps. A modulation depth up to 60% was achieved with a low laser fluence of 63.5 μJ cm^{-2}. The features reported in these works, together with the high THz electron mobility of Cd_3As_2, are appealing for compact, energy efficient and tunable nanophotonic and plasmonic devices operating in the infrared and THz regions.

5.2.8. $PtTe_2$ and $PtSe_2$ (TDS)

Politano et al.[164] and Ghosh et al.[165] studied the plasmonic response of $PtTe_2$ single crystals and thin films. They reported Dirac plasmons in the infrared, together with other spectral features attributed to interband transitions. Hu et al. reported plasmon propagation at mid infrared frequencies in $PtTe_2$ nanoflakes and nanoribbons. The observed response was shown to originate from the excitation of both free carriers and Dirac fermions.[166] Wong et al. showed that $PtSe_2$, while

**ADVANCED
SCIENCE NEWS**

www.advancedsciencenews.com

**ADVANCED
FUNCTIONAL
MATERIALS**

www.afm-journal.de

being a semimetal, displays a high refractive index (near 5) in the mid infrared. This property was shown to enable waveguiding of mid infrared light in nanostructures.[167] These results are appealing for the manipulation of infrared light on nanophotonic platforms.

5.2.9. WTe$_2$ (Weyl Semimetal)

Wang et al. reported tunable far infrared plasmons in WTe$_2$ microribbons. Such plasmons were tuned by changing temperature and material thickness.[168] By designing arrays of WTe$_2$ microdisks and rectangles, Wang et al. reported anisotropic 2D plasmons with a hyperbolic dispersion.[169] Such anisotropy was shown to be tunable by varying the temperature. These features, taken altogether, are appealing for the active manipulation of infrared light on nanophotonic platforms.

5.2.10. TaAs and NbAs (Weyl Semimetals)

Chiarello et al. reported mid infrared tunable plasmons in TaAs and NbAs single crystals.[170] The plasmonic features were shown to change in presence of an adsorbate. This points at the interest of using such materials for infrared plasmonic sensor applications.

6. Thermal Devices

The process of thermal photons generation from TIs usually share similar physics as photon absorption by optoelectronic devices made of TIs. In describing the thermal emission from conventional planar emitting surfaces, one usually chooses the eigenstates of the thermal photons to be linear polarized as $|p\rangle$ and $|s\rangle$. Controlling the polarization state of thermal radiation usually relies on structured thermal emitters that can support polarized resonances or interactions. Specifically, circularly polarized thermal emission would require chiral photonic crystals or metasurfaces with breaking mirror symmetry. However, planner thermal emitters made of TI could radiate thermal photons that carry a net spin angular momentum.[171,172] Consider a thermal emitter proposed in ref. [172] shown in **Figure 8**a that consists of a semi-infinite TI substrate with a thin magnetic film on top that induces a time-reversal symmetry breaking and leads to a quantum Hall states with a topological magnetoelectric effect. If one denotes the polarization of thermal photon in the $|p\rangle - |s\rangle$ basis as $\cos\frac{\theta}{2}|p\rangle - e^{i\phi}\sin\frac{\theta}{2}|s\rangle$, then the polarization of the eigenstates of emitted photons can be represented on a Poincaré sphere as shown in Figure 8b. In the case of conventional planner thermal emitters, the eigenstates can be represented as point A and A' along the Z axis. In the case where the loss of the TI is infinitesimal, due to the magnetically induced magnetoelectric effect, the eigenstates shift along the equator
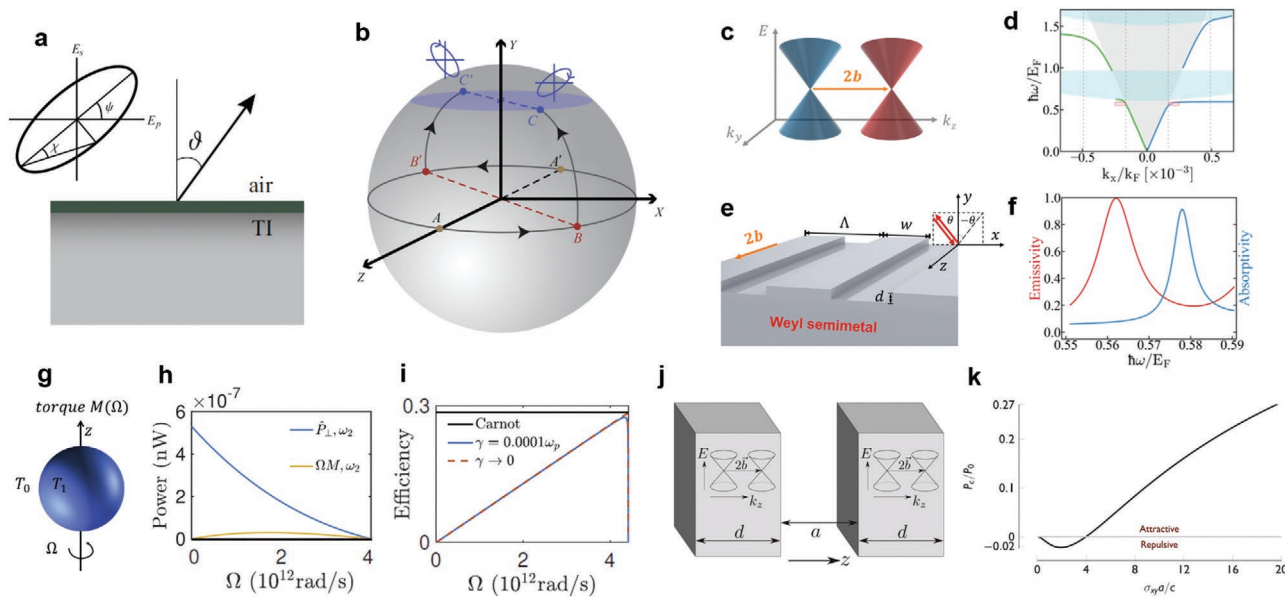

Figure 8. a) Schematic of a semi-infinite slab of a TI thermal emitter with a thin magnetic film atop. b) Poincare sphere of the eigenstates of thermal photons. The Y coordinate directly gives the spin angular momentum of the photon in unit of ℏ. Reproduced with permission.[172] Copyright 2019, Wiley-VCH. c) Schematic of a band structure of a magnetic Weyl semimetal with two Weyl nodes separated by **2b** in momentum space. d) Dispersion of the nonreciprocal surface plasmon dispersion of the Weyl semimetal. The gray region is the light cone of vacuum. The continuum of bulk modes are shown with the blue region. The red region denotes the surface plasmons used for nonreciprocal thermal properties. The gray dashed lines are the boundaries of the Brillouin zones. $k_F = E_F/\hbar\nu_F$ is the Fermi wavevector. e) Schematic of a nonreciprocal thermal emitter based on a Weyl semimetal photonic crystal. Reproduced with permission.[173] f) Emissivity and absorptivity spectrum in $\theta = 80°$ direction. Reproduced with permission.[173] Copyright 2020, American Chemical Society. g) Schematic a gyrotropic nano-sphere at a temperature T_1, surrounded by vacuum at temperature T_0. h) The net power radiated from the particle to free space ($\hat{p}$) and the mechanical work (ΩM) output as a function of rotating frequency Ω when $T_1 = 70K$ and $T_0 = 50K$. Both quantities are dominated by the resonance at ω_2. i) The efficiency of the heat engine compared to the Carnot efficiency when the scattering rate of the material changes. Reproduced with permission.[180] Copyright 2021, American Chemical Society. j) Schematic of two Weyl semimetals separated by a distance in vacuum. The insert shows the Weyl cones and their separations in momentum space. k) The normalized Casimir force between two semi-infinite bulk Weyl semimetals. Reproduced with permission.[181] Copyright 2015, American Physical Society.

to a diametrically opposite pair B and B'. Additional loss finally shifts the points off the equator to points C and C', representing polarization states with nonzero spin angular momentum.

Besides the polarization modification, thermal emitters based on TMs could also break the reciprocity in thermal radiation. Conventional thermal emitters are reciprocal and they obey Kirchhoff's law of thermal radiation stating that for a given direction, polarization, and frequency, the emissivity and the absorptivity are equal. However, with magnetic TMs that break reciprocity, Kirchhoff's law can be violated. For example, based on the large nonreciprocal effect in magnetic Weyl semimetals, Zhao et al.[173] proposed a broadband thermal emitter that achieves complete violation of Kirchhoff's law at room-temperatures. Consider a case where the Weyl cone separation is along the z direction as indicated in Figure 8c. Due to the reciprocity breaking effect, the left-propagating ($-x$ direction) and right-propagating ($+x$ direction) surface plasmon polaritons of the Weyl semimetals have different dispersions, as shown in Figure 8d . A thermal emitter based on periodic grating structure shown in Figure 8e can utilize different branches of surface plasmon polaritons for the emission and absorption process, and ,therefore, result in significant violation of Kirchhoff's law for p-polarized thermal radiation, as indicated in Figure 8f. Tsurimaki et al.[174,175] investigated a similar effect taking into account the Fermi-arc surface state and number of Weyl node pairs included. Violation of Kirchhoff's law can be obtained also in transmissive emitters. As shown in ref. [176], one can achieve complete absorption of normally incident light on one side of emitter, whereas the emission is completely on the other side of the emitter. Compared to previous proposals for nonreciprocal thermal emitters that are based on magnetooptical materials under external magnetic field,[177,178] magnetic Weyl semimetals provide intrinsic time-reversal breaking effect that does not require any external field. Meanwhile, compared to magnetooptical materials, magnetic Weyl semimetals provide a much stronger nonreciprocal effect. As discussed previously, thermal emission from magnetic TMs that break time-reversal symmetry could possess a nonzero spin angular momentum. As detailed in Khandekar et al.,[179] Kirchhoff's law is also violated for these chiral thermal emitters.

Since the thermal photons from TMs can carry nonzero spin angular momentum, the emission of such photons can result in an backaction torque on the thermal emitter.[171,182] In ref. [171], Maghrebi et al. discussed this fluctuation-driven torque for a TI thin film out of thermal equilibrium with a cold environment. In ref. [180], Guo and Fan showed that this effect can be used to create a heat engine and discussed conditions at which the efficiency of this heat engine can approach the Carnot efficiency. Due to the backaction torque, a particle initially at rest will start to rotate and eventually reach a steady-state angular frequency because of the vacuum friction (Figure 8g). Therefore, the particle can act as a heat engine that converts thermal energy from random thermal fluctuations to kinetic energy in the rotation of the particle. In Figure 8h,i, the authors show the power and efficiency of a such heat engine when the particle has an ideal optical property. With a temperature ($T_1 = 70$ K) higher than the ambient ($T_0 = 50$ K), the sphere emits radiative heat flux (P) and produces work (ΩM) when the angular

frequency Ω is greater than zero and smaller than the steady state angular frequency, when the torque becomes zero. Both heat flux and the work are dominated by the resonance at ω_2. With the choice of the material property, the efficiency of the heat engine can approach Carnot efficiency in the limit of large cyclotron frequency and small material loss. We note that the authors demonstrate the effect with a magneto-optical particle. But as the authors pointed out, TMs with broken time-reversal symmetry, such as magnetic Weyl semimetals, could provide larger nonreciprocal effect and therefore offer exciting opportunities to construct such heat engines.

Along with the exciting opportunities in heat transfer and energy conversion, TIs also provide an effective way to create repulsive Casimir force, a long sought after effect.[183–185] In ref. [181], Wilson et al. reported repulsive Casimir force between semi-infinite magnetic Weyl semimetals when the separation of the two semimetals is smaller than the trap distance $a \le 4c/\sigma_{xy}$, where c is the speed of light in vacuum, and σ_{xy} is the bulk hall conductivity of Weyl semimetals. As illustrated in Figure 8k, the Casimir force becomes attractive once the distance is greater than the trap distance, which is on the order of micrometers for magnetic Weyl semimetals provided that the momentum separation of the two Weyl nodes b is ≈ 1 nm^{-1}. For the same reason, repulsive Casimir force can also exist between other TMs such as 2D Hall materials[184] and time-reversal broken TIs (by magnetic field, for example).[185,186]

7. Nonlinear Optics

Nonlinear optics is a broad research category which focuses on the light-matter interaction beyond linear response,[187] and has stimulated lots of technological innovations. One example is the frequency down conversion from light to current, such as bulk photovoltaic effect discussed in the former chapter and THz pulse generation via optical rectification. In this section, we will mainly introduce other interesting and active branches; high harmonic generation, saturable absorption, and population inversion in TMs.

7.1. High Harmonic Generation

High harmonic generation (HHG) is a frequency multiplication of incident pumping electromagnetic wave. HHG up to tens of orders has been first studied in gaseous media[188] and utilized to generate extreme ultraviolet or soft X-ray pulses in attosecond science[189] as well as in laser-based ARPES. Recently, HHG has also been found in semiconductors[190,191] and attracted a great deal of interests for potential applications to generate solid-based stable extreme ultraviolet light source,[192] image electric fields in devices with high speed,[193] reveal Berry curvature in solids,[194] and reconstruct crystal band structure.[195] Besides the practical applications, HHG is challenging our understandings of the strong light–matter interaction and the nonlinear electromagnetic responses in solids.[193,196] Microscopically, the light field induces i) the intraband current from the carrier acceleration and ii) the interband polarization from the electron tunneling between the valance and the conduction bands. Both of

them could contribute to HHG. The studies of HHG have been mainly conducted by using strong near- and mid-infrared laser pulses, that is, 1–10 micrometers in wavelength and 30–300 THz in frequency. For lower frequency in far-infrared or THz region, however, harmonic generation is hardly observed due to lack of nonlinear crystals and light source until recently.

In this sense, linear band dispersion systems have received recent attention because they may realize efficient frequency conversion in the THz regime. Let us consider a simplest picture. In a linear band system $E(\mathbf{k}) = \pm \hbar v_F |\mathbf{k}|$ with a small Fermi energy, an intense sinusoidal THz field could drive Dirac/Weyl fermions to oscillate back and forth inside the Dirac/Weyl cone.[197] As the velocity suddenly changes sign across the Dirac/Weyl node, the system could carry a square-wave-like intraband current $\mathbf{j} \approx -\mathbf{v}_F \mathrm{sgn}(\sin \omega t)$ (**Figure 9**a). Here sgn is the sign function. This unusual intraband current intrinsically carries the odd-order harmonics such as 3ω, 5ω, 7ω, ..., even in a relatively low field strength (Figure 9b). In contrast, conventional materials whose bands are well approximated by quadratic dispersion would carry intraband currents proportional to driving sinusoidal electric field. That is, no HHG will be generated by the intraband current unless electrons are accelerated into nonparabolic dispersion region.

Graphene is a prototypical 2D linear band system and has been first predicted as a platform for efficient THz HHG.[197] Recent THz and mid-infrared HHG experiments have demonstrated efficient odd-order harmonic generations in this monolayer material.[202–204] Remarkably, the nonlinear THz susceptibility χ in graphene was demonstrated to be extremely large,

7–18 orders of magnitude larger than typical materials for third, fifth, and seventh order harmonics.[204] However, the conversion efficiency of high harmonics in graphene is severely limited by its 2D character with a vanishingly small thickness L because the field strength of high harmonics is proportional to χL.

Two recent experiments of Cd_3As_2 thin films have demonstrated that TMs could be a new and promising solid-state system for THz HHG.[198,205] Cd_3As_2 is a prototypical TDS with 3D linear band dispersion.[20,206,207] As shown in Figure 9c, pumped by an quasi-monochromatic THz field at $\omega = 0.8$ THz, Cd_3As_2 radiates THz third harmonics at 3ω. Figure 9d shows that THz third harmonic increases as E_{pump}^3 in the lower pumping field strength, and it saturates to follow $E_{pump}^{2.1}$ when the field strength is beyond 20 kV cm^{-1}, indicating the nonlinear interaction goes beyond the perturbative regime. Higher orders up to seventh have also been observed under a stronger field.[205] Figure 9c shows the transmission of fundamental wave (ω) is smaller in Cd_3As_2 than in graphene because incident THz wave is mostly reflected at the surface of Cd_3As_2, and the 20-kV cm^{-1} incident field in air is reduced to a 4 kV cm^{-1} inside the film with 240-nm thickness. Nevertheless, the observed harmonics magnitude in Cd_3As_2 film is much larger than in graphene, demonstrating an extremely efficient frequency conversion.[198]

Further THz pump-probe experiments and theoretical analysis demonstrate that the THz HHG in Cd_3As_2 originates from the intraband acceleration of electrons in the linear band dispersion as the picture we discussed earlier.[198,205] Such an intraband acceleration and the nonthermal electron distribution of
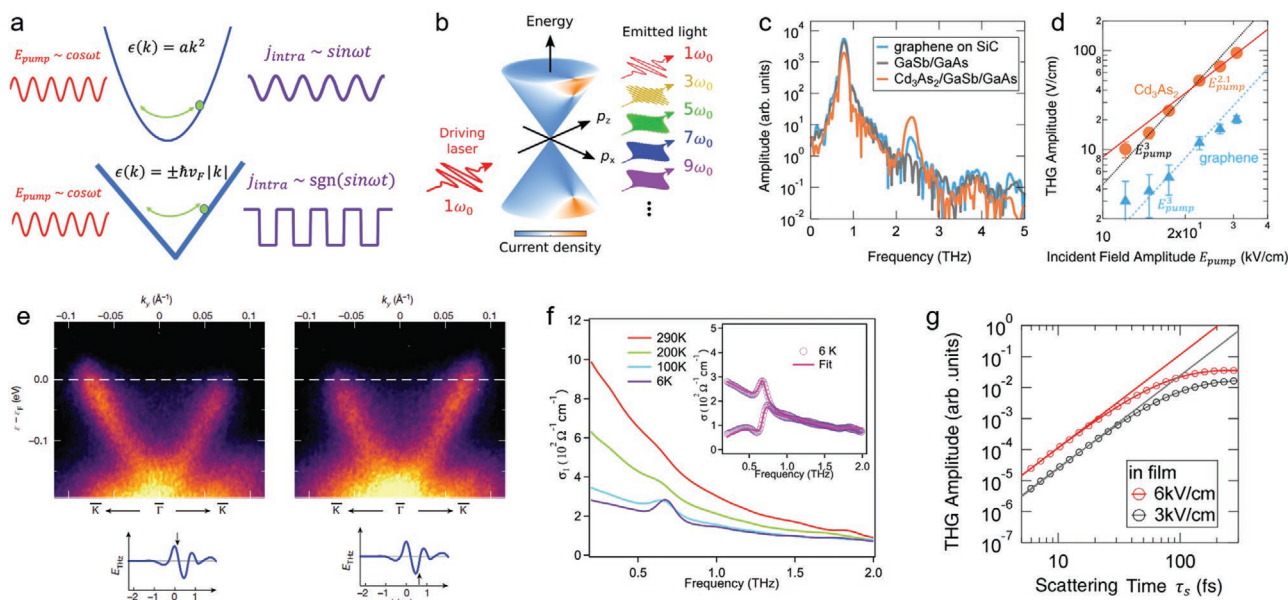

Figure 9. a) Schematics for intraband current in a parabolic band (upper) and in a linear band (lower). The driven intraband current will be proportional to the driving sinusoidal electric field in the parabolic band and the square wave in the linear band. b) A schematic for high harmonic generations in 3D TDSs. The fundamental wave frequency is ω_0. The high harmonic generation frequency are $(2n+1)\omega_0$. Here n is positive integer. Reproduced with permission.[199] Copyright 2020, American Physical Society. c) THz third harmonic generation in Cd_3As_2 film and graphene. The fundamental pumping frequency is 0.8 THz. The third harmonic generation appears at 2.4 THz. d) THz third harmonic generation amplitude as a function of incident pumping field strengths. Reproduced with permission.[198] Copyright 2020, American Physical Society. e) THz-pumped APRES study for the topological surface state in a TI Bi_2Te_3. The accelerated electrons form quite nonthermal distribution in momentum space depending on the sign of the THz field, which is the microscopic origin of THz HHG. Reproduced with permission.[201] Copyright 2018, Springer Nature. f) THz conductivity of the Cd_3As_2 film at different temperatures. Reproduced with permission.[201] Copyright 2020, American Chemical Society. g) THz third harmonic generation amplitude simulated as a function of transport scattering time with a pumping field strength of 3 and 6 kV cm^{-1}. The calculation is performed in the frame of intraband acceleration model.

Dirac electrons in momentum space have been directly monitored by a recent THz-pumped ARPES work in a TI Bi_2Te_3[201] (Figure 9e). The efficient acceleration is closely related with the long carrier scattering time, which could be as long as ≈1 ps in TIs due to the spin-momentum locking.[201] In the Dirac semimetal Cd_3As_2, the Drude scattering is found to be around 0.6 THz (Figure 9f), that is, scattering time ≈250 fs at room temperature.[200] Such a low scattering rate would allow the electrons experience less scattering during the laser-driven acceleration process, leading to a large nonperturbative nonlinear current even under a few kV cm^{-1} field (Figure 9g). It is worth to note that the scattering and recombination of carriers in graphene are much faster than in usual TMs, and the origin of THz HHG there was explained by a thermodynamic picture.[204]

THz HHG has also been observed in TIs pumped by THz[208] and mid infrared pulses.[209] Very recently, an exciting progress was made by using phase-locked intense pulses centering at 25 to 42 THz to explore HHG in a TI Bi_2Te_3.[210] When the pumping frequency is tuned below the bulk bandgap, the photon energy is not large enough to excite interband electron-hole pairs effectively. Instead, the THz field will primarily accelerate surface Dirac fermions and stimulate a large nonlinear surface current, which finally dominates the HHG process. Interestingly, the HHG spectrum can be continuously shifted by tuning the phase of the incident field and the peaks can be located at the noninteger multiples of the driving frequency. Such a tunability of the HHG peaks have been known to appear slightly at the highest orders in conventional materials when the pump field is strong enough to accelerate the carriers far away from the Fermi surface,[191] but in the Dirac system a moderate driving field is enough because of the extremely high optical nonlinearity near the Dirac node. This new finding will bring up more insights on the nonperturbative nonlinear responses in TMs.

We would like to point out that large optical nonlinearity and THz THG have been observed in superconductors too, and are used as a probe on the collective excitation of superconducting order parameters.[211–213] However, THz HHG in superconductors needs cryogenic low temperature, which limits their practical applications. In contrast, Dirac semimetals can radiate THz HHG efficiently even at room temperature because it relies on the linear band dispersion. This pioneering feature provides enormous opportunity to conduct further in-depth research and explore the practical applications of THz HHG without a cryostat. It is also noteworthy that the nonlinear optical response can be further strengthened by local field enhancement on metamaterial structure. A recent work shows the THz third-order nonlinearity in graphene could be enhanced up to 50 times through a grating metamaterial.[214] Similar techniques could also be implemented in TMs for efficient HHG.

Besides the THz frequency, TMs also show significant harmonic generation in higher frequency region. Recent second harmonic generation studies of a Weyl semimetal TaAs from mid-infrared to visible frequency region have shown at least ten times larger nonlinear coefficient in TaAs than in those typical semiconductors such as GaAs, ZnTe, and $PbTiO_3$.[25,215] Such a high-frequency HHG response is directly related with the Berry curvature in momentum space rather than the pure Weyl nature.[216] The large optical nonlinearity in TaAs would be useful for THz wave generation and optoelectronic devices.

The research of HHG in TMs, especially of the THz HHG in TMs, is still in its early stage. More further works, including experimental and theoretical, are highly demanding.[199,217,218] As there exists a large number of material candidates for TMs,[7] they could afford more space to optimize the HHG yield and to explore the underlying HHG mechanism. Furthermore, the progress of sample growth in the thin-film geometry would provide far more options to explore HHG by fabricating devices to tune their electronic properties. Works like gating-dependent studies of THz HHG in TMs would be interesting extensions of current THz HHG research in TMs.

7.2. Saturable Absorption

HHG is essentially a result of coherent nonlinear light–matter interaction, that is, it occurs only during light irradiation and does not require dephasing and dissipation processes. On the other hand, TMs have also been interesting in terms of incoherent aspect of nonlinear responses which occurs after electrons are excited. The Pauli exclusion principle inhibits additional excitation of electrons to the occupied states. This Pauli blocking can reduce the interband absorption till the photoexcited carriers relax, which leads to saturable absorption, that is, absorption in matter becomes smaller as the pumping fluence becomes stronger.[187] Saturable absorption is actually important for passive optical switches to stabilize ultrafast pulse emission in mode-locked lasers.[222] Semiconductor saturable absorber mirrors (SESAMs) have been extensively utilized for near-infrared pulsed lasers, but recent increasing demands of mid-infrared pulsed lasers requires other types of materials with large optical nonlinearity in the lower frequency region. In this regards, TMs such as 3D Dirac semimetals can be ideal large-area saturable absorbers in mid-infrared region.

Figure 10a shows the transmittance of a 400 nm-thick Cd_3As_2 thin film excited by a mid-infrared laser of 3.2 μm.[219] One can see that the transmittance gradually increases as the pump fluence increases, demonstrating a modulation depth of 4.4% and a saturation intensity of 0.78 GW cm^{-2}. As shown in Figure 10b, the Cd_3As_2 film was implemented as a robust saturable absorber in a mid-infrared fiber laser system[219] and mode-locking pulsed emission was clearly demonstrated (Figure 10c). One important parameter for saturable absorbers is the lifetime of photo-excited carriers. It can be tuned from several to sub picoseconds by element doping,[219] which may meet different demands for laser development. A saturable absorber using Cd_3As_2 has also been realized in near infrared[223] and the modulation depth could be actively tuned from 33% to 76% by using current-induced heating.[224] Considering TMs have quite similar 3D linear band dispersion and ultrafast charge relaxation dynamics,[221] these results indicate TMs could be promising material candidates to develop ultrafast optical switch and compact mid-infrared short pulse laser.

7.3. Stimulated Emission

Finally, we would like to introduce another aspect of nonlinear responses if electrons are photo-excited in matter more
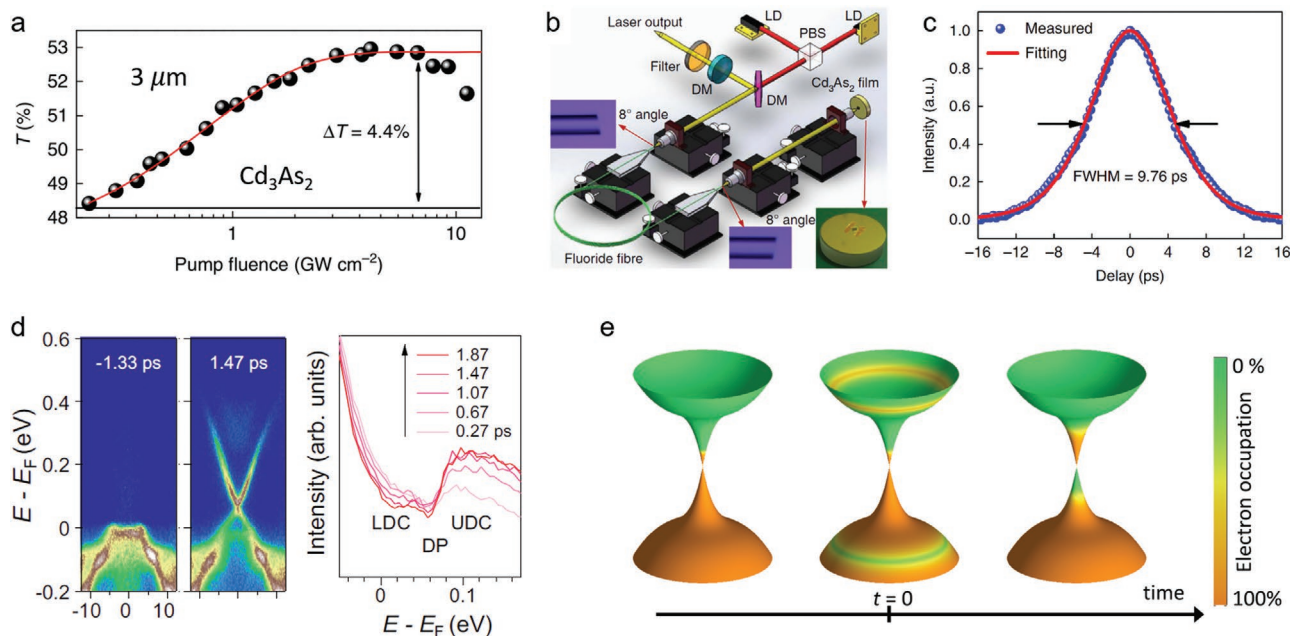
Figure 10. a) Transmittance of Cd_3As_2 thin film as a function of laser pump fluence at 3.2 μm. b) A schematic of mid-infrared fibre laser including a Cd_3As_2 thin film as a saturable absorber. LD, PBS, and DM are diode laser, polarized beam splitter, and dichroic mirror, respectively. c) Autocorrelation signal of the pulsed laser output at 2.8 μm with FWHM of 9.8 ps, corresponding to a pulse duration of 6.3 ps. Reproduced with permission.[219] Copyright 2017, Springer Nature. d) Time-resolved ARPES study for population inversion in photoexcited TI. Reproduced with permission.[220] Copyright 2019, American Physical Society. e) Schematics of possible ultrafast distribution of photoexcited electrons in 3D TMs when the interband relaxation is slow. Reproduced with permission.[221] Copyright 2017, American Institute of Physics.

strongly. The absorption further decreases and may go to zero and may even change its sign, that is, the optical conductivity can be negative, which corresponds to amplification of the incident light rather than absorption in matter. This is called stimulated emission and is known as the emission mechanism of lasers. In equilibrium, the interband absorption is always larger than the stimulated emission. When the high-density electrons are photo-excited, however, the electrons in the conduction and valence bands may reach quasi-equilibrium independently with distinct chemical potentials if the interband recombination is slow enough (Figure 10e). In this case, the population of electrons can be inverted and the stimulated emission may occur. Graphene has been predicted as a gain medium for low-frequency lasing because of its gapless nature.[225] An ultrafast near-infrared pump–probe study of graphene has revealed a decrease in reflectivity at 930–1070 nm after pumped by 800 nm, indicating negative optical conductivity.[226] However, population inversion in graphene could take place only within 100–200 fs after the photoexcitation because of the fast Auger scattering and electron–hole recombination.[226,227] In addition, the Fermi energy in large-area graphene usually shifts a few hundreds of meV with charge doping, resulting in the Pauli blocking in far-infrared region. Therefore, it is very difficult to realize stimulated emission around THz frequency in graphene. Many time-resolved studies in graphene show that the transient THz conductivity is always positive, that is, loss is still larger than absorption, although the change of the conductivity can be positive or negative depending on circumstances.[228,229]

For another Dirac system with a much longer relaxation time, time-resolved ARPES studies for a Dirac surface state in a TI $(Sb_{1-x}Bi_x)_2Te_3$ have clearly demonstrated the population inversion near the Dirac node with the recombination time of 10 ps even at room temperature (Figure 10d).[220,230] Note that, however, the population inversion is not sufficient for light amplification because the intraband Drude absorption of carriers also occurs in such a low frequency region and competes with the interband stimulated emission. In addition, the Dirac electrons in TIs are confined on the atomically thin surface, and the bulk states tend to intervene if the Fermi level is close to bulk states, which makes the stimulated emission from the Dirac surface states very challenging.

To overcome this situation and realize a low-frequency stimulated emission, one needs to look for other material candidates with a long relaxation time and a large volume. One important example is the narrow-gap semiconductors $Hg_{1-x}Cd_xTe$, which shows the Lifshitz transition to TI by elemental substitution.[231] The stimulated emission in $Hg_{1-x}Cd_xTe$ has been known to occur in mid infrared by observing lasing threshold of luminescence at 2–5 μm,[232] and recently it was extended for longer wavelength to 20 mm (15 THz) below 100 K by using quantum well heterostructures.[233] Recently the stimulated cyclotron emission was also demonstrated under magnetic field with tunable frequency at a few THz,[234] as a candidate for Landau-level laser.[235] Other types of 3D TMs such as Cd_3As_2 may be also candidates for the low-energy stimulated emission. Importantly, in contrast to graphene, the Auger scattering is suppressed in systems with 3D linear dispersion,[236] which can lead to the long relaxation time of photoexcited carriers of several picoseconds in 3D TMs.[219,221,237,238] It may be possible to spot usable 3D TMs to realize population inversion and stimulated emission, and build a mid-infrared laser with broad bandwidth.

8. Outlook/Future Perspectives

As surveyed throughout this review, TMs provide a unique platform to realize next generation optoelectronic devices. However, much remains to be done to optimize the structure and integration of current TMs for an enhanced device performance. Furthermore, many unexplored TMs certainly remain to be considered. Recent analysis predicts that about 24% of all known materials have topological properties. This fact, combined with recent advances in different areas of materials science, such as 2D materials with atomic-scale thicknesses and organic–inorganic materials, could unleash vast and unexplored possibilities for many areas of science and engineering including optoelectronics. Linking TMs to optoelectronic devices and applications necessitates producing and depositing high-quality materials. Advanced synthesis techniques with extremely high level of precision and accuracy need to be further improved to obtain atomic-level deposition control. Such a control will opens up routes for tunable phase transition, dynamic symmetry manipulation, and on-demand dimensionality transformation. Although recent efforts have demonstrated the possibility of synthesizing atomically thin large-scale 2D TMs, realizing devices based on 2D TMs is currently lacking. Another possibility, yet to be experimentally demonstrates, is the realization of TMs in battery energy storage systems such as solar panels. Additionally, TMs may provide opportunities in quantum computing, improved light emitting systems, and multimedia content such as augmented reality and virtual reality. Future advancements to the technical challenges of low-energy photodetection can greatly benefit from the opportunities opened up by topological physics. The research depth and breadth of TMs, including theoretical and experimental, are still developing rapidly. The nonlinear optical effects in TMs, besides using to develop optical functional devices, are also found to enable to identify topological phases. For example, in non-centrosymmetric TIs, the HHG spectrum is predicted to reveal the topological features hiding behind the shift vectors, leading to π phase difference in the HHG spectrum from the HHG in topological trivial insulators.[239] In the meanwhile, more novel topological entities, such as higher-fold chiral fermions, topological Weyl loops and topological axion states, have been discovered in TMs recently. The entanglement between topological phases and other symmetry-broken ordered states, for example, superconductivity, charge density wave, and magnetism, is found to breed new physics and exotic phenomena. All these exciting progresses will afford much vaster stage to realize advanced functional devices.

Appendix: Fabrication of TMs; Crystals, thin Films, Nanostructures and Metamaterials

Herein, the methods used for the fabrication of TMs as crystals, thin films, nanostructures and metamaterials are shortly discussed. Examples of such methods, structure type, material composition and the corresponding references are given in **Table A1**.

Crystals: The growth of TM crystals has been achieved by several means, such as the Bridgman or Czochralski methods, the metal flux/evaporation/chemical vapor transport method, or the floating zone method.[240] These methods, in addition to be among the less expensive ones, enable the fabrication of single crystals with controlled composition and sizes reaching the cm scale.

Thin Films: Thin films can be obtained from the corresponding crystals by mechanical exfoliation. Such approach enables producing films with thickness down to few-nm. Their surface area, remains, however, limited by the size of the initial crystal. The so-obtained films can be transferred onto a chosen substrate, where it can be integrated to produce a device (e.g., covered with electronic contact layers, connected with planar electrodes).

Deposition techniques, such as MBE, evaporation, ALD, PLD, or magnetron sputtering are also broadly used to produce TMs as thin films. MBE enables preparing single-crystal films with a finely tuned thickness (thicknesses from few-nm to 500 nm have been reported) and composition (binary to quaternary compounds have been reported). Films with good crystal quality and a controlled thickness down to few-nm can also be achieved by evaporation with slow deposition rate or ALD. Magnetron sputtering, PVD and PLD have also been used to prepare crystalline and amorphous films. The films grown by these different deposition techniques cover areas above the cm scale. They enable a strong binding of the films with the substrate, thus enabling a practical fabrication of flexible or integrated devices. Their main drawbacks are their cost and the need of specific crystalline substrates enabling epitaxial growth, especially when MBE is concerned.

Nanostructures and Metamaterials: The growth of large amounts of nanostructures such as nanoplates, nanowires, nanoribbons, nanoflowers, or nanosheets is enabled by various techniques such as the solvothermal method, solution growth possibly assisted by microwaves, hydrothermal, VS, VLS, SVS, CVD, vapor transport, and hot pressing of powders. These techniques, however, do not enable controlling the nanostructure shape, size, and organization with the accuracy needed to produce metamaterials.

In contrast, using suitable lithography techniques such EBL or FIB to structure TM crystals or thin films brings the necessary accuracy to produce metamaterials. These techniques have been harnessed to fabricate nanogratings, periodic arrays of nanoribbons, nanogrooves, nanoslits, nanorings, nanolenses, or bullseye structures. However, they suffer from their high cost and their limitation to small-area designs. Further exploring the combination of film and crystal growth with top-down structuring is needed to produce, at a low cost, large-area metamaterials based on TMs. A step toward this aim has been made by depositing TM films by ALD onto laser-written 3D polymer-based photonic crystal templates.

Conflict of Interest

The authors declare no conflict of interest.

Table A1. Examples of fabrication methods of TMs as crystals, thin films, nanostructures, and metamaterials. The examples are grouped as a function of the structure. For each case, the fabrication method, material composition, and reference are given. Abbreviations: QL = quintuple layer, MBE = molecular beam epitaxy, ALD = atomic layer deposition, PLD = pulsed laser deposition, PVD = physical vapor deposition, VS = vapor–solid, VLS = vapor–liquid–solid, SVS= solid–vapor–solid, CVD = chemical vapor deposition, FIB = focused ion beam, EBL = electron beam lithography, RIE = reactive ion etching.

Type	Method	Composition	Ref.
Crystal	Floating zone method	$Bi_{1.5}Sb_{0.5}Te_{3-x}Se_x$	[152]
Crystal	Evaporation	$PtTe_2$	[164]
Crystal	Evaporation	$PtTe_2$	[165]
Crystal	Chemical vapor transport	TaAs, NbAs	[170]
Thin film	Exfoliation	Bi_2Te_3	[29]
Thin film	Exfoliation	Bi_2Se_3	[33]
Thin film <100 nm	Exfoliation	Bi_2Se_3	[38]
Thin film 15–50 nm	Exfoliation	Bi_2Te_2Se	[118]
Thin film	Exfoliation	$Bi_{1.5}Sb_{0.5}Te_{1.8}Se_{1.2}$	[119]
Thin film	Exfoliation	WTe_2	[169]
Thin film 50 nm	MBE	Bi_2Se_3	[114]
Thin film	MBE	Bi_2Se_3	[158]
Thin film	MBE	$(Bi_{1-x}Sb_x)_2Se_3$	[36]
Thin film 20 nmm	MBE	$(Bi_{1-x}Sb_x)_2Te_3$	[108]
Thin film 8 nm (coated)	MBE	$(Bi_{1-x}Sb_x)_2Te_3$	[117]
Thin film 10–20 QL	MBE	$(Bi_{1-x}Sb_x)_2Te_3$	[123]
Thin film 100 nm	MBE	$(Bi_{0.75}In_{0.25})_2Te_3$	[115]
Thin film	MBE	$(Bi_{1-x}In_x)_2Te_3$	[113]
Thin film 50 nm	MBE	$(Bi_{0.5}In_{0.5})_2Se_3$	[120]
Thin film few-QL	MBE	Na_3Bi	[41]
Thin film	MBE	$Cr_{0.15}(Bi_{0.1}Sb_{0.9})_{1.85}Te_3$	[40]
Thin film	MBE	Cd_3As_2	[27]
Thin film 500 nm	MBE	Cd_3As_2	[52]
Thin film	MBE	Cd_3As_2	[37]
Thin film 2–8 QL	Evaporation (sequential)	Bi_2Se_3	[32]
Thin film 10 nm	Evaporation	Bi_2Se_3	[104]
Thin film 70 nm	Evaporation (sequential)	Sb_2Te_3	[109]
Thin film 50–80 nm	Magnetron sputtering	Sb_2Te_3 (C-doped)	[121]
Thin film 50	ALD	Sb_2Te_3	[146]
Thin film (amorphous)	PLD	Bi_2Te_3	[160]
Thin film 17–260 nm	PVD	$Bi_xSb_{xy}Te_z$	[138]
Nanoplates 8–22 nm	Solvothermal	Bi_2Se_3	[106]
Nanoplates	Solvothermal	Bi_2Te_3	[39]
Nanoplates	Solvothermal	Bi_2Te_3	[126]
Nanoplates 10–20 nm	Solvothermal	Bi_2Te_3	[142]
Nanoribbons	Solution process	Bi_2Te_3	[28]
Nanopowder	Solution process	$Bi_{1.6}Sb_{0.4}Te_3$	[111]
Nanoflowers	Microwave-assisted growth	Bi_2Se_3	[144]
Nanoplates	Hydrothermal, VS, VLS	Bi_2Se_3 w/organics	[137]
Nanowires	VLS	Bi_2Te_3	[116]
Nanowires	SVS	Bi_2Se_3	[34]
Nanowires	CVD	Bi_2Se_3	[35]
Nanosheets 3-200 QL	Hot pressing	Bi_2Se_3	[105]
Nanoplatelets	Vapor transport	Bi_2Se_3	[148]

**ADVANCED
SCIENCE NEWS**

www.advancedsciencenews.com

**ADVANCED
FUNCTIONAL
MATERIALS**

www.afm-journal.de

Table A1. Continued.

Type	Method	Composition	Ref.
Nanoslits in crystal	FIB	$Bi_{1.5}Sb_{0.5}Te_{1.8}Se_{1.2}$	[124]
Nanocones in crystal	FIB	$(Bi_{1-x}Sb_x)_2(Te_ySe_{1-y})_3$	[125]
Nanogrooves in thin film	Melting-cooling, exfoliation, FIB	Sb_2Te_3	[145]
Nanogrooves in thin film	MBE, lithography	$(Bi_{1-x}In_x)_2Se_3$	[127]
Nanogrooves in thin film	MBE, EBL	Bi_2Se_3	[128]
Nanorings in thin film	MBE, EBL	Bi_2Se_3	[154]
Nanostripes in thin film	MBE, EBL	Bi_2Se_3	[155]
Nanoribbons in thin film	MBE, EBL	Bi_2Se_3	[157]
Nanoribbons in thin film	MBE, EBL	Bi_2Se_3	[151]
Nanoribbons in thin film	MBE, EBL	$(Bi_{1-x}In_x)_2Se_3$	[156]
Nanogrooves in amorphous thin film	Evaporation, FIB	Bi_xTe_y	[136]
Nanogratings in thin film	CVD, EBL	WTe_2	[168]
Nanolens	ALD, FIB	Sb_2Te_3	[149]
Metasurface	RIE	Bi_2Se_3	[122]
Bullseye structure in film	Exfoliation, FIB	Bi_2Te_3	[143]
3D metamaterial	Laser writing, ALD	Sb_2Te_3	[131]

Author Contributions

H.C. wrote most of the Introduction, and Photodetectors sections. B.C. and R.M. wrote the Nonlinear Optics section. B.Z., V.A., and S.F. wrote the Thermal Devices section and helped with the Introduction and Photodetectors sections. J.T. and H.C. wrote the Nanophotonic and Plasmonic Devices. O.F.S. and H.C. wrote the Field Effect Transistors section. All authors contributed to the discussion of content, preparation, revision, and editing of the manuscript and edited the manuscript prior to submission.

[1] H. Gao, J. W. Venderbos, Y. Kim, A. M. Rappe, *Annu. Rev. Mater. Res.* **2019**, *49*, 153.

[2] B. Yan, C. Felser, *Annu. Rev. Condens. Matter Phys.* **2017**, *8*, 337.

[3] M. Z. Hasan, J. E. Moore, *Annu. Rev. Condens. Matter Phys.* **2011**, *2*, 55.

[4] P. Liu, J. R. Williams, J. J. Cha, *Nat. Rev. Mater.* **2019**, *4*, 479.

[5] X.-L. Qi, S.-C. Zhang, *Rev. Mod. Phys.* **2011**, *83*, 1057.

[6] M. Z. Hasan, C. L. Kane, *Rev. Mod. Phys.* **2010**, *82*, 3045.

[7] N. P. Armitage, E. J. Mele, A. Vishwanath, *Rev. Mod. Phys.* **2018**, *90*, 015001.

[8] M. Z. Hasan, S.-Y. Xu, G. Bian, *Phys. Scr.* **2015**, *T164*, 014001.

[9] M. Z. Hasan, S.-Y. Xu, I. Belopolski, S.-M. Huang, *Annu. Rev. Condens. Matter Phys.* **2017**, *8*, 289.

[10] L. Fu, C. L. Kane, E. J. Mele, *Phys. Rev. Lett.* **2007**, *98*, 106803.

[11] H. Zhang, C.-X. Liu, X.-L. Qi, X. Dai, Z. Fang, S.-C. Zhang, *Nat. Phys.* **2009**, *5*, 438.

[12] Y. Chen, J. G. Analytis, J.-H. Chu, Z. Liu, S.-K. Mo, X.-L. Qi, H. Zhang, D. Lu, X. Dai, Z. Fang, S. C. Zhang, I. R. Fisher, Z. Hussain, Z.-X. Shen, *Science* **2009**, *325*, 178.

[13] D. Hsieh, Y. Xia, L. Wray, D. Qian, A. Pal, J. H. Dil, J. Osterwalder, F. Meier, G. Bihlmayer, C. L. Kane, Y. S. Hor, R. J. Cava, M. Z. Hasan, *Science* **2009**, *323*, 919.

[14] K. S. Novoselov, A. K. Geim, S. V. Morozov, D. Jiang, Y. Zhang, S. V. Dubonos, I. V. Grigorieva, A. A. Firsov, *Science* **2004**, *306*, 666.

[15] C. L. Kane, E. J. Mele, *Phys. Rev. Lett.* **2005**, *95*, 226801.

[16] J. Chen, H. J. Qin, F. Yang, J. Liu, T. Guan, F. M. Qu, G. H. Zhang, J. R. Shi, X. C. Xie, C. L. Yang, K. H. Wu, Y. Q. Li, L. Lu, *Phys. Rev. Lett.* **2010**, *105*, 176602.

[17] L. Fu, *Phys. Rev. Lett.* **2011**, *106*, 106802.

[18] Y. Tanaka, Z. Ren, T. Sato, K. Nakayama, S. Souma, T. Takahashi, K. Segawa, Y. Ando, *Nat. Phys.* **2012**, *8*, 800.

[19] Z. K. Liu, B. Zhou, Y. Zhang, Z. J. Wang, H. M. Weng, D. Prabhakaran, S.-K. Mo, Z. X. Shen, Z. Fang, X. Dai, Z. Hussain, Y. L. Chen, *Science* **2014**, *343*, 864.

[20] M. Neupane, S. Xu, R. Sankar, N. Alidoust, G. Bian, C. Liu, I. Belopolski, T. Chang, H. Jeng, H. Lin, A. Bansil, F. Chou, M. Z. Hasan, *Nat. Commun.* **2014**, *5*, 3786.

[21] S.-Y. Xu, I. Belopolski, N. Alidoust, M. Neupane, G. Bian, C. Zhang, R. Sankar, G. Chang, Z. Yuan, C.-C. Lee, S.-M. Huang, H. Zheng, J. Ma, D. S. Sanchez, B. Wang, A. Bansil, F. Chou, P. P. Shibayev, H. Lin, S. Jia, M. Z. Hasan, *Science* **2015**, *349*, 613.

[22] B. Q. Lv, H. M. Weng, B. B. Fu, X. P. Wang, H. Miao, J. Ma, P. Richard, X. C. Huang, L. X. Zhao, G. F. Chen, Z. Fang, X. Dai, T. Qian, H. Ding, *Phys. Rev. X* **2015**, *5*, 031013.

[23] K. Kuroda, T. Tomita, M.-T. Suzuki, C. Bareille, A. A. Nugroho, P. Goswami, M. Ochi, M. Ikhlas, M. Nakayama, S. Akebi, R. Noguchi, R. Ishii, N. Inami, K. Ono, H. Kumigashira, A. Varykhalov, T. Muro, T. Koretsune, R. Arita, S. Shin, T. Kondo, S. Nakatsuji, *Nat. Mater.* **2015**, *16*, 1090.

[24] S. Borisenko, D. Evtushinsky, Q. Gibson, A. Yaresko, K. Koepernik, T. Kim, M. Ali, J. van den Brink, M. Hoesch, A. Fedorov, E. Haubold, Y. Kushnirenko, I. Soldatov, R. Schäfer, R. J. Cava, *Nat. Commun.* 10, 3424.

[25] L. Wu, S. Patankar, T. Morimoto, N. L. Nair, E. Thewalt, A. Little, J. G. Analytis, J. E. Moore, J. Orenstein, *Nat. Phys.* **2017**, *13*, 350.

**ADVANCED
SCIENCE NEWS**

www.advancedsciencenews.com

**ADVANCED
FUNCTIONAL
MATERIALS**

www.afm-journal.de

[26] M. Fischetti, L. Wang, B. Yu, C. Sachs, P. Asbeck, Y. Taur, M. Rodwell, in *2007 IEEE Int. Electron Devices Meeting*, IEEE, Piscataway, NJ **2007**, pp. 109–112.

[27] O. F. Shoron, M. Goyal, B. Guo, D. A. Kealhofer, T. Schumann, S. Stemmer, *Adv. Electron. Mater.* **2020**, *6*, 2000676.

[28] F. Xiu, L. He, Y. Wang, L. Cheng, L.-T. Chang, M. Lang, G. Huang, X. Kou, Y. Zhou, X. Jiang, Z. Chen, J. Zou, A. Shailos, K. L. Wang, *Nat. Nanotechnol.* **2011**, *6*, 216.

[29] H. Liu, P. D. Ye, *Appl. Phys. Lett.* **2011**, *99*, 052108.

[30] J.-M. Yan, Z.-X. Xu, T.-W. Chen, M. Xu, C. Zhang, X.-W. Zhao, F. Liu, L. Guo, S.-Y. Yan, G.-Y. Gao, F.-F. Wang, J.-X. Zhang, S.-N. Dong, X.-G. Li, H.-S. Luo, W. Zhao, R.-K. Zheng, *ACS Appl. Mater. Interfaces* **2019**, *11*, 9548.

[31] M. Fang, Z. Wang, H. Gu, B. Song, Z. Guo, J. Zhu, X. Chen, C. Zhang, H. Jiang, S. Liu, *Appl. Phys. Lett.* **2021**, *118*, 191101.

[32] B. C. Park, T.-H. Kim, K. I. Sim, B. Kang, J. W. Kim, B. Cho, K.-H. Jeong, M.-H. Cho, J. H. Kim, *Nat. Commun.* **2015**, *6*, 6552.

[33] S. Cho, N. P. Butch, J. Paglione, M. S. Fuhrer, *Nano Lett.* **2011**, *11*, 1925.

[34] H. Zhu, C. A. Richter, E. Zhao, J. E. Bonevich, W. A. Kimes, H.-J. Jang, H. Yuan, H. Li, A. Arab, O. Kirillov, J. E. Maslar, D. E. Ioannou, Q. Li, *Sci. Rep.* **2013**, *3*, 1757.

[35] H. Zhu, C. A. Richter, S. Yu, H. Ye, M. Zeng, Q. Li, *Appl. Phys. Lett.* **2019**, *115*, 073107.

[36] Y.-H. Liu, C.-W. Chong, C.-M. FanChiang, J.-C.-A. Huang, H.-C. Han, Z. Li, H. Qiu, Y.-C. Li, C.-P. Liu, *ACS Appl. Mater. Interfaces* **2017**, *9*, 12859.

[37] O. F. Shoron, T. Schumann, M. Goyal, D. A. Kealhofer, S. Stemmer, *Appl. Phys. Lett.* **2019**, *115*, 062101.

[38] H. Steinberg, D. R. Gardner, Y. S. Lee, P. Jarillo-Herrero, *Nano Lett.* **2010**, *10*, 5032.

[39] Y. Wang, F. Xiu, L. Cheng, L. He, M. Lang, J. Tang, X. Kou, X. Yu, X. Jiang, Z. Chen, J. Zou, K. L. Wang, *Nano Lett.* **2012**, *12*, 1170.

[40] Z. Zhang, X. Feng, M. Guo, K. Li, J. Zhang, Y. Ou, Y. Feng, L. Wang, X. Chen, K. He, X. Ma, Q. Xue, Y. Wang, *Nat. Commun.* **2014**, *5*, 4915.

[41] J. L. Collins, A. Tadich, W. Wu, L. C. Gomes, J. N. Rodrigues, C. Liu, J. Hellerstedt, H. Ryu, S. Tang, S.-K. Mo, S. Adam, S. A. Yang, M. S. Fuhre, M. T. Edmonds, *Nature* **2018**, *564*, 390.

[42] H. Yuan, H. Liu, H. Shimotani, H. Guo, M. Chen, Q. Xue, Y. Iwasa, *Nano Lett.* **2011**, *11*, 2601.

[43] J. Liu, D. Vanderbilt, *Phys. Rev. B* **2013**, *88*, 224202.

[44] T. Schumann, L. Galletti, D. A. Kealhofer, H. Kim, M. Goyal, S. Stemmer, *Phys. Rev. Lett.* **2018**, *120*, 016801.

[45] M. Goyal, L. Galletti, S. Salmani-Rezaie, T. Schumann, D. A. Kealhofer, S. Stemmer, *APL Mater.* **2018**, *6*, 026105.

[46] J. Ikeda, K. Fujiwara, J. Shiogai, T. Seki, K. Nomura, K. Takanashi, A. Tsukazaki, *Commun. Mater.* **2021**, *2*, 18.

[47] H. Qiao, J. Yuan, Z. Xu, C. Chen, S. Lin, Y. Wang, J. Song, Y. Liu, Q. Khan, H. Y. Hoh, C.-X. Pan, S. Li, Q. Bao, *ACS Nano* **2015**, *9*, 1886.

[48] K. Zheng, L.-B. Luo, T.-F. Zhang, Y.-H. Liu, Y.-Q. Yu, R. Lu, H.-L. Qiu, Z.-J. Li, J. A. Huang, *J. Mater. Chem. C* **2015**, *3*, 9154.

[49] J. Yao, Z. Zheng, G. Yang, *J. Mater. Chem. C* **2016**, *4*, 7831.

[50] Q. Wang, C.-Z. Li, S. Ge, J.-G. Li, W. Lu, J. Lai, X. Liu, J. Ma, D.-P. Yu, Z.-M. Liao, D. Sun, *Nano Lett.* **2017**, *17*, 834.

[51] F. Wang, L. Li, W. Huang, L. Li, B. Jin, H. Li, T. Zhai, *Adv. Funct. Mater.* **2018**, *28*, 1802707.

[52] H. T. Chorsi, S. Yue, P. P. Iyer, M. Goyal, T. Schumann, S. Stemmer, B. Liao, J. A. Schuller, *Adv. Opt. Mater.* **2020**, *8*, 1901192.

[53] V. M. Fridkin, A. A. Grekov, P. V. Ionov, A. I. Rodin, E. A. Savchenko, K. A. Mikhailina, *Ferroelectrics* **1974**, *8*, 433.

[54] A. Zenkevich, Y. Matveyev, K. Maksimova, R. Gaynutdinov, A. Tolstikhina, V. Fridkin, *Phys. Rev. B* **2014**, *90*, 161409.

[55] A. M. Cook, B. M. Fregoso, F. de Juan, S. Coh, J. E. Moore, *Nat. Commun.* **2017**, *8*, 14176.

[56] M.-M. Yang, D. J. Kim, M. Alexe, *Science* **2018**, *360*, 904.

[57] C.-K. Chan, N. H. Lindner, G. Refael, P. A. Lee, *Phys. Rev. B* **2017**, *95*, 041104.

[58] G. B. Osterhoudt, L. K. Diebel, M. J. Gray, X. Yang, J. Stanco, X. Huang, B. Shen, N. Ni, P. J. W. Moll, Y. Ran, K. S. Burch, *Nat. Mater.* **2019**, *18*, 471.

[59] J. E. Sipe, A. I. Shkrebtii, *Phys. Rev. B* **2000**, *61*, 5337.

[60] S. Chi, Z. Li, Y. Xie, Y. Zhao, Z. Wang, L. Li, H. Yu, G. Wang, H. Weng, H. Zhang, J. Wang, *Adv. Mater.* **2018**, *30*, 1801372.

[61] J. Yang, W. Yu, Z. Pan, Q. Yu, Q. Yin, L. Guo, Y. Zhao, T. Sun, Q. Bao, K. Zhang, *Small* **2018**, *14*, 1802598.

[62] M. Yang, J. Wang, J. Han, J. Ling, C. Ji, X. Kong, X. Liu, Z. Huang, J. Gou, Z. Liu, F. Xiu, Y. Jiang, *ACS Photonics* **2018**, *5*, 3438.

[63] S. Liu, Z. Huang, H. Qiao, R. Hu, Q. Ma, K. Huang, H. Li, X. Qi, *Nanoscale Adv.* **2020**, *2*, 906.

[64] M. Yang, Q. Han, X. Liu, J. Han, Y. Zhao, L. He, J. Gou, Z. Wu, X. Wang, J. Wang, *Adv. Funct. Mater.* **2020**, *30*, 1909659.

[65] E. J. König, H.-Y. Xie, D. A. Pesin, A. Levchenko, *Phys. Rev. B* **2017**, *96*, 075123.

[66] K. Sun, S.-S. Sun, L.-L. Wei, C. Guo, H.-F. Tian, G.-F. Chen, H.-X. Yang, J.-Q. Li, *Chin. Phys. Lett.* **2017**, *34*, 117203.

[67] F. de Juan, A. G. Grushin, T. Morimoto, J. E. Moore, *Nat. Commun.* **2017**, *8*, 15995.

[68] L. E. Golub, E. L. Ivchenko, B. Z. Spivak, *JETP Lett.* **2017**, *105*, 782.

[69] Q. Ma, S.-Y. Xu, C.-K. Chan, C.-L. Zhang, G. Chang, Y. Lin, W. Xie, T. Palacios, H. Lin, S. Jia, P. A. Lee, P. Jarillo-Herrero, N. Gedik, *Nat. Phys.* **2017**, *13*, 842.

[70] Y. Zhang, H. Ishizuka, J. van den Brink, C. Felser, B. Yan, N. Nagaosa, *Phys. Rev. B* **2018**, *97*, 241118.

[71] Z. Ji, G. Liu, Z. Addison, W. Liu, P. Yu, H. Gao, Z. Liu, A. M. Rappe, C. L. Kane, E. J. Mele, R. Agarwal, *Nat. Mater.* **2019**, *18*, 955.

[72] J. Ma, Q. Gu, Y. Liu, J. Lai, P. Yu, X. Zhuo, Z. Liu, J.-H. Chen, J. Feng, D. Sun, *Nat. Mater.* **2019**, *18*, 476.

[73] I. Sodemann, L. Fu, *Phys. Rev. Lett.* **2015**, *115*, 216806.

[74] H. Rostami, M. Polini, *Phys. Rev. B* **2018**, *97*, 195151.

[75] Y. Zhang, Y. Sun, B. Yan, *Phys. Rev. B* **2018**, *97*, 041101.

[76] Y. Gao, F. Zhang, W. Zhang, *Phys. Rev. B* **2020**, *102*, 245116.

[77] Z. Ni, K. Wang, Y. Zhang, O. Pozo, B. Xu, X. Han, K. Manna, J. Paglione, C. Felser, A. G. Grushin, F. de Juan, E. J. Mele, L. Wu, *Nat. Commun.* **2021**, *12*, 154.

[78] J. Yao, J. Shao, Y. Wang, Z. Zhao, G. Yang, *Nanoscale* **2015**, *7*, 12535.

[79] H. Zhang, X. Zhang, C. Liu, S.-T. Lee, J. Jie, *ACS Nano* **2016**, *10*, 5113.

[80] H. Zhang, B. Man, Q. Zhang, *ACS Appl. Mater. Interfaces* **2017**, *9*, 14067.

[81] L. Hao, Y. Du, Z. Wang, Y. Wu, H. Xu, S. Dong, H. Liu, Y. Liu, Q. Xue, Z. Han, K. Yan, M. Dong, *Nanoscale* **2020**, *12*, 7358.

[82] J. Liu, X. Li, H. Wang, G. Yuan, A. Suvorova, S. Gain, Y. Ren, W. Lei, *ACS Appl. Mater. Interfaces* **2020**, *12*, 31810.

[83] T. Jiang, Y. Zang, H. Sun, X. Zheng, Y. Liu, Y. Gong, L. Fang, X. Cheng, K. He, *Adv. Opt. Mater.* **2017**, *5*, 1600727.

[84] J. Yao, Z. Zheng, G. Yang, *Adv. Funct. Mater.* **2017**, *27*, 1701823.

[85] J. Lai, X. Liu, J. Ma, Q. Wang, K. Zhang, X. Ren, Y. Liu, Q. Gu, X. Zhuo, W. Lu, Y. Wu, Y. Li, J. Feng, S. Zhou, J.-H. Chen, D. Sun, *Adv. Mater.* **2018**, *30*, 1707152.

[86] J. Lai, Y. Liu, J. Ma, X. Zhuo, Y. Peng, W. Lu, Z. Liu, J. Chen, D. Sun, *ACS Nano* **2018**, *12*, 4055.

[87] M. Yang, J. Wang, Y. Zhao, L. He, C. Ji, X. Liu, H. Zhou, Z. Wu, X. Wang, Y. Jiang, *ACS Nano* **2018**, *13*, 755.

[88] M. Yang, J. Wang, Y. Yang, Q. Zhang, C. Ji, G. Wu, Y. Su, J. Gou, Z. Wu, K. Yuan, F. Xiu, Y. Jiang, *J. Phys. Chem. Lett.* **2019**, *10*, 3914.

[89] H. Liu, X. Zhu, X. Sun, C. Zhu, W. Huang, X. Zhang, B. Zheng, Z. Zou, Z. Luo, X. Wang, D. Li, A. Pan, *ACS Nano* **2019**, *13*, 13573.

**ADVANCED
SCIENCE NEWS**

www.advancedsciencenews.com

**ADVANCED
FUNCTIONAL
MATERIALS**

www.afm-journal.de

[90] W. Zhou, J. Chen, H. Gao, T. Hu, S. Ruan, A. Stroppa, W. Ren, *Adv. Mater.* **2019**, *31*, 1804629.

[91] G. B. Osterhoudt, L. K. Diebel, M. J. Gray, X. Yang, J. Stanco, X. Huang, B. Shen, N. Ni, P. J. Moll, Y. Ran, K. S. Burch, *Nat. Mater.* **2019**, *18*, 471.

[92] H. Zhang, Z. Song, D. Li, Y. Xu, J. Li, C. Bai, B. Man, *Appl. Surf. Sci.* **2020**, *509*, 145290.

[93] J. Lai, J. Ma, Y. Liu, K. Zhang, X. Zhuo, J.-H. Chen, S. Zhou, D. Sun, *2D Mater.* **2020**, *7*, 034003.

[94] M. Zhao, J. Su, Y. Zhao, P. Luo, F. Wang, W. Han, Y. Li, X. Zu, L. Qiao, T. Zhai, *Adv. Funct. Mater.* **2020**, *30*, 1909849.

[95] M. Yang, Y. Yang, Q. Liu, H. Zhou, J. Han, X. Xie, F. Xiu, J. Gou, Z. Wu, Z. Hu, T. Yu, J. Wang, Y. Jiang, *J. Mater. Chem. C* **2020**, *8*, 16024.

[96] M. Li, Z. Wang, X. P. Gao, Z. Zhang, *J. Phys. Chem. C* **2020**, *124*, 10135.

[97] Y. Zhang, L. Tang, K. S. Teng, *Nanotechnology* **2020**, *31*, 304002.

[98] X. Zhang, R. Pan, Y. Yang, X. Liu, J. Han, H. Zhou, J. Gou, F. Xiu, J. Wang, *Opt. Mater.* **2021**, *111*, 110699.

[99] H. Weng, C. Fang, Z. Fang, B. A. Bernevig, X. Dai, *Phys. Rev. X* **2015**, *5*, 011029.

[100] X. Zhang, R. Pan, Y. Yang, Q. Han, X. Liu, C. Zhang, H. Zhou, J. Han, J. Gou, J. Wang, *Adv. Photonics Res.* **2021**, *2*, 2000194.

[101] T. J. Yoo, W. S. Kim, K. E. Chang, C. Kim, M. G. Kwon, J. Y. Jo, B. H. Lee, *Nanomaterials* **2021**, *11*, 755.

[102] S. Huang, X. Xu, *Adv. Opt. Mater.* **2021**, *9*, 2002210.

[103] T. Wei, X. Wang, Q. Yang, Z. He, P. Yu, Z. Xie, H. Chen, S. Li, S. Wu, *ACS Appl. Mater. Interfaces* **2021**, *13*, 22757.

[104] H. Peng, W. Dang, J. Cao, Y. Chen, D. Wu, W. Zheng, H. Li, Z.-X. Shen, Z. Liu, *Nat. Chem.* **2012**, *4*, 281.

[105] N. Hussain, Q. Zhang, J. Lang, R. Zhang, M. Muhammad, K. Huang, T. Cosseron De Villenoisy, H. Ya, A. Karim, H. Wu, *Adv. Opt. Mater.* **2018**, *6*, 1701322.

[106] Y. Liu, K. Tom, X. Wang, C. Huang, H. Yuan, H. Ding, C. Ko, J. Suh, L. Pan, K. A. Persson, J. Yao, *Nano Lett.* **2016**, *16*, 488.

[107] J. Jeon, K. Yu, J. Kim, J. Moon, S. Oh, E. Choi, *Phys. Rev. B* **2019**, *100*, 195110.

[108] W. S. Whitney, V. W. Brar, Y. Ou, Y. Shao, A. R. Davoyan, D. N. Basov, K. He, Q.-K. Xue, H. A. Atwater, *Nano Lett.* **2017**, *17*, 255.

[109] S. H. Park, J. Chae, K. S. Jeong, T.-H. Kim, H. Choi, M.-H. Cho, I. Hwang, M.-H. Bae, C. Kang, *Nano Lett.* **2015**, *15*, 3820.

[110] X. Li, R. Liu, H. Xie, Y. Zhang, B. Lyu, P. Wang, J. Wang, Q. Fan, Y. Ma, S. Tao, S. Xiao, X. Yu, Y. Gao, J. He, *Opt. Express* **2017**, *25*, 18346.

[111] C. Song, H. Zhang, L. Jin, X. Ma, Y. Zou, L. Shi, Y. Xu, *Adv. Opt. Mater.* **2020**, *8*, 1901618.

[112] S. Sim, N. Koirala, M. Brahlek, J. H. Sung, J. Park, S. Cha, M.-H. Jo, S. Oh, H. Choi, *Phys. Rev. B* **2015**, *91*, 235438.

[113] S. Sim, M. Brahlek, N. Koirala, S. Cha, S. Oh, H. Choi, *Phys. Rev. B* **2014**, *89*, 165137.

[114] L. Luo, X. Yang, X. Liu, Z. Liu, C. Vaswani, D. Cheng, M. Mootz, X. Zhao, Y. Yao, C.-Z. Wang, K.-M. Ho, I. E. Perakis, M. Dobrowolska, J. K. Furdyna, J. Wang, *Nat. Commun.* **2019**, *10*, 607.

[115] T. Shi, K. Kushnir, Z. Wang, S. Law, L. V. Titova, *ACS Photonics* **2020**, *7*, 2778.

[116] D. Park, K. Jeong, I. Maeng, D. Kim, H. Kwon, S.-B. Hong, J.-H. Kim, C.-S. Kee, C. Kang, M.-H. Cho, *Adv. Opt. Mater.* **2019**, *7*, 1900621.

[117] K. N. Okada, N. Ogawa, R. Yoshimi, A. Tsukazaki, K. S. Takahashi, M. Kawasaki, Y. Tokura, *Phys. Rev. B* **2016**, *93*, 081403.

[118] P. K. Venuthurumilli, X. Wen, V. Iyer, Y. P. Chen, X. Xu, *ACS Photonics* **2019**, *6*, 2492.

[119] A. M. Dubrovkin, G. Adamo, J. Yin, L. Wang, C. Soci, Q. J. Wang, N. I. Zheludev, *Adv. Opt. Mater.* **2017**, *5*, 1600768.

[120] Z. Wang, T. P. Ginley, S. V. Mambakkam, G. Chandan, Y. Zhang, C. Ni, S. Law, *Phys. Rev. Mater.* **2020**, *4*, 115202.

[121] Y. Meng, J. K. Behera, S. Wen, R. E. Simpson, J. Shi, L. Wu, Z. Song, J. Wei, Y. Wang, *Adv. Opt. Mater.* **2018**, *6*, 1800360.

[122] Y. Hu, M. Tong, X. Cheng, J. Zhang, H. Hao, J. You, X. Zheng, T. Jiang, *ACS Photonics* **2021**, *8*, 771.

[123] Y. Pan, Q.-Z. Wang, A. L. Yeats, T. Pillsbury, T. C. Flanagan, A. Richardella, H. Zhang, D. D. Awschalom, C.-X. Liu, N. Samarth, *Nat. Commun.* **2017**, *8*, 1037.

[124] J.-Y. Ou, J.-K. So, G. Adamo, A. Sulaev, L. Wang, N. I. Zheludev, *Nat. Commun.* **2014**, *5*, 5139.

[125] Z. Yue, B. Cai, L. Wang, X. Wang, M. Gu, *Sci. Adv.* **2016**, *2*, 3e1501536.

[126] M. Zhao, J. Zhang, N. Gao, P. Song, M. Bosman, B. Peng, B. Sun, C.-W. Qiu, Q.-H. Xu, Q. Bao, K. P. Loh, *Adv. Mater.* **2016**, *28*, 3138.

[127] S. Sim, J. Park, N. Koirala, S. Lee, M. Brahlek, J. Moon, M. Salehi, J. Kim, S. Cha, J. H. Sung, M.-Ho Jo, S. Oh, H. Choi, *ACS Photonics* **2016**, *3*, 1426.

[128] M. Autore, H. Engelkamp, F. D'Apuzzo, A. D. Gaspare, P. D. Pietro, I. L. Vecchio, M. Brahlek, N. Koirala, S. Oh, S. Lupi, *ACS Photonics* **2015**, *2*, 1231.

[129] D. Piccinotti, B. Gholipour, J. Yao, K. F. MacDonald, B. E. Hayden, N. I. Zheludev, *Adv. Opt. Mater.* **2018**, *6*, 22.

[130] J. Toudert, R. Serna, M. G. Pardo, N. Ramos, R. J. Peláez, B. Maté, *Opt. Express* **2018**, *26*, 34043.

[131] E. Goi, Z. Yue, B. P. Cumming, M. Gu, *Phys. Status Solidi A* **2018**, *215*, 1800152.

[132] J. Yin, H. N. Krishnamoorthy, G. Adamo, A. M. Dubrovkin, Y. Chong, N. I. Zheludev, C. Soci, *NPG Asia Mater.* **2017**, *9*, e425.

[133] J. Toudert, R. Serna, *Opt. Mater. Express* **2017**, *7*, 2299.

[134] J. Toudert, *Nanotechnol. Rev.* **2014**, *3*, 223.

[135] J. Toudert, R. Serna, *Opt. Mater. Express* **2016**, *6*, 2434.

[136] D. Piccinotti, B. Gholipour, J. Yao, K. F. Macdonald, B. E. Hayden, N. I. Zheludev, *Opt. Express* **2018**, *26*, 20861.

[137] J. J. Cha, K. J. Koski, K. C. Huang, K. X. Wang, D. Luo, W. Kong, Z. Yu, S. Fan, M. L. Brongersma, Y. Cui, *Nano Lett.* **2013**, *13*, 5913.

[138] D. Piccinotti, B. Gholipour, J. Yao, K. F. MacDonald, B. E. Hayden, N. I. Zheludev, *Adv. Mater.* **2019**, *31*, 14.

[139] Z. Yue, Q. Chen, A. Sahu, X. Wang, M. Gu, *Mater. Res. Express* **2017**, *4*, 126403.

[140] Z. Yue, G. Xue, J. Liu, Y. Wang, M. Gu, *Nat. Commun.* **2017**, *8*, 15354.

[141] M. Esslinger, R. Vogelgesang, N. Talebi, W. Khunsin, P. Gehring, S. De Zuani, B. Gompf, K. Kern, *ACS Photonics* **2014**, *1*, 1285.

[142] U. Saleem, F. A. Permatasari, F. Iskandar, T. Ogi, K. Okuyama, Y. Darma, M. Zhao, K. P. Loh, A. Rusydi, P. Coquet, M. D. Birowosuto, H. Wang, *Adv. Opt. Mater.* **2017**, *5*, 1700176.

[143] Q. Yan, X. Li, B. Liang, *Materials* **2020**, *13*, 1531.

[144] J. Guozhi, W. Peng, Z. Yanbang, C. Kai, *Sci. Rep.* **2016**, *6*, 25884.

[145] H. Lu, Z. Yue, Y. Li, Y. Zhang, M. Zhang, W. Zeng, X. Gan, D. Mao, F. Xiao, T. Mei, W. Zhao, X. Wang, M. Gu, J. Zhao, *Light: Sci. Appl.* **2020**, *9*, 191.

[146] H. Lu, S. Dai, Z. Yue, Y. Fan, H. Cheng, J. Di, D. Mao, E. Li, T. Mei, J. Zhao, *Nanoscale* **2019**, *11*, 4759.

[147] N. Talebi, C. Ozsoy-Keskinbora, H. M. Benia, K. Kern, C. T. Koch, P. A. Van Aken, *ACS Nano* **2016**, *10*, 6988.

[148] R. Lingstädt, N. Talebi, M. Hentschel, S. Mashhadi, B. Gompf, M. Burghard, H. Giessen, P. A. van Aken, *Commun. Mater.* **2021**, *2*, 5.

[149] Z. Yue, H. Ren, S. Wei, J. Lin, M. Gu, *Nat. Commun.* **2018**, *9*, 4413.

[150] X. Sun, G. Adamo, M. Eginligil, H. N. Krishnamoorthy, N. I. Zheludev, C. Soci, *Sci. Adv.* **2021**, *7*, eabe5748.

[151] P. Di Pietro, M. Ortolani, O. Limaj, A. Di Gaspare, V. Giliberti, F. Giorgianni, M. Brahlek, N. Bansal, N. Koirala, S. Oh, P. Calvani, S. Lupi, *Nat. Nanotechnol.* **2013**, *8*, 556.

[152] A. Kogar, S. Vig, A. Thaler, M. Wong, Y. Xiao, D. Reig-i Plessis, G. Cho, T. Valla, Z. Pan, J. Schneeloch, R. Zhong, G. D. Gu, T. L. Hughes, G. J. MacDougall, T.-C. Chiang, P. Abbamonte, *Phys. Rev. Lett.* **2015**, *115*, 257402.

[153] T. P. Ginley, S. Law, *Adv. Opt. Mater.* **2018**, *6*, 1800113.

[154] M. Autore, F. D'Apuzzo, A. Di Gaspare, V. Giliberti, O. Limaj, P. Roy, M. Brahlek, N. Koirala, S. Oh, F. J. Garcia de Abajo, S. Lupi, *Adv. Opt. Mater.* **2015**, *3*, 1257.

[155] C. In, S. Sim, B. Kim, H. Bae, H. Jung, W. Jang, M. Son, J. Moon, M. Salehi, S. Y. Seo, A. Soon, M.-H. Ham, H. Lee, S. Oh, D. Kim, M.-H. Jo, H. Choi, *Nano Lett.* **2018**, *18*, 734.

[156] M. Autore, F. Giorgianni, F. D'Apuzzo, A. Di Gaspare, I. L. Vecchio, M. Brahlek, N. Koirala, S. Oh, U. Schade, M. Ortolani, S. Lupi, *Nanoscale* **2016**, *8*, 4667.

[157] P. Di Pietro, N. Adhlakha, F. Piccirilli, A. Di Gaspare, J. Moon, S. Oh, S. Di Mitri, S. Spampinati, A. Perucchi, S. Lupi, *Phys. Rev. Lett.* **2020**, *124*, 226403.

[158] S. Sim, H. Jang, N. Koirala, M. Brahlek, J. Moon, J. H. Sung, J. Park, S. Cha, S. Oh, M.-H. Jo, J.-H. Ahn, H. Choi, *Nat. Commun.* **2015**, *6*, 8814.

[159] J. Lu, H. Liu, Y. Yu, Z. Ni, X. Zhang, *Appl. Phys. Lett.* **2019**, *115*, 251109.

[160] Z. Chai, X. Hu, Y. Zhao, Y. Wu, S. Wang, H. Yang, Q. Gong, *AIP Adv.* **2018**, *8*, 065324.

[161] H. Krishnamoorthy, G. Adamo, J. Yin, V. Savinov, N. Zheludev, C. Soci, *Nat. Commun.* **2020**, *11*, 1692.

[162] G. Jia, Z. Huang, Y. Zhou, H. Wang, Y. Zhang, X. Miao, *Phys. Chem. Chem. Phys.* **2021**, *23*, 13128.

[163] Z. Dai, M. Manjappa, Y. Yang, T. C. W. Tan, B. Qiang, S. Han, L. J. Wong, F. Xiu, W. Liu, R. Singh, *Adv. Funct. Mater.* **2021**, *31*, 2011011.

[164] A. Politano, G. Chiarello, B. Ghosh, K. Sadhukhan, C.-N. Kuo, C. S. Lue, V. Pellegrini, A. Agarwal, *Phys. Rev. Lett.* **2018**, *121*, 086804.

[165] B. Ghosh, F. Alessandro, M. Zappia, R. Brescia, C.-N. Kuo, C. S. Lue, G. Chiarello, A. Politano, L. S. Caputi, A. Agarwal, A. Cupolillo, *Phys. Rev. B* **2019**, *99*, 045414.

[166] X. Hu, K. P. Wong, L. Zeng, X. Guo, T. Liu, L. Zhang, Q. Chen, X. Zhang, Y. Zhu, K. H. Fung, S. P. Lau, *ACS Nano* **2020**, *14*, 6276.

[167] K. P. Wong, X. Hu, T. W. Lo, X. Guo, K. H. Fung, Y. Zhu, S. P. Lau, *Adv. Opt. Mater.* **2021**, *9*, 2100294.

[168] C. Wang, Y. Sun, S. Huang, Q. Xing, G. Zhang, C. Song, F. Wang, Y. Xie, Y. Lei, Z. Sun, H. Yan, *Phys. Rev. Appl.* **2021**, *15*, 014010.

[169] C. Wang, S. Huang, Q. Xing, Y. Xie, C. Song, F. Wang, H. Yan, *Nat. Commun.* **2020**, *11*, 1158.

[170] G. Chiarello, J. Hofmann, Z. Li, V. Fabio, L. Guo, X. Chen, S. D. Sarma, A. Politano, *Phys. Rev. B* **2019**, *99*, 121401.

[171] M. F. Maghrebi, A. V. Gorshkov, J. D. Sau, *Phys. Rev. Lett.* **2019**, *123*, 055901.

[172] E. Khan, E. E. Narimanov, *Phys. Rev. B* **2019**, *100*, 081408.

[173] B. Zhao, C. Guo, C. A. C. Garcia, P. Narang, S. Fan, *Nano Lett.* **2020**, *20*, 1923.

[174] Y. Tsurimaki, X. Qian, S. Pajovic, F. Han, M. Li, G. Chen, *Phys. Rev. B* **2020**, *101*, 165426.

[175] S. Pajovic, Y. Tsurimaki, X. Qian, G. Chen, *Phys. Rev. B* **2020**, *102*, 165417.

[176] Y. Park, V. S. Asadchy, B. Zhao, C. Guo, J. Wang, S. Fan, *ACS Photonics* **2021**, *8*, 2417.

[177] L. Zhu, S. Fan, *Phys. Rev. B* **2014**, *90*, 220301.

[178] B. Zhao, Y. Shi, J. Wang, Z. Zhao, N. Zhao, S. Fan, *Opt. Lett.* **2019**, *44*, 4203.

[179] C. Khandekar, F. Khosravi, Z. Li, Z. Jacob, *New J. Phys.* **2020**, *22*, 123005.

[180] Y. Guo, S. Fan, *ACS Photonics* **2021**, *8*, 1623.

[181] J. H. Wilson, A. A. Allocca, V. Galitski, *Phys. Rev. B* **2015**, *91*, 235115.

[182] A. Ott, P. Ben-Abdallah, S.-A. Biehs, *Phys. Rev. B* **2018**, *97*, 205414.

[183] T. H. Boyer, *Phys. Rev. A* **1974**, *9*, 2078.

[184] W.-K. Tse, A. H. MacDonald, *Phys. Rev. Lett.* **2012**, *109*, 236806.

[185] A. G. Grushin, A. Cortijo, *Phys. Rev. Lett.* **2011**, *106*, 020403.

[186] P. Rodriguez-Lopez, A. G. Grushin, *Phys. Rev. Lett.* **2014**, *112*, 056804.

[187] R. W. Boyd, *Nonlinear Optics*, Academic Press, San Diego, CA **2008**.

[188] M. Ferray, A. L'Huillier, X. F. Li, L. A. Lompre, G. Mainfray, C. Manus, *J. Phys. B: Atom., Mol. Opt. Phys.* **1988**, *21*, L31.

[189] M. Drescher, R. Hentschel, Michael aad Kienberger, G. Tempea, C. Spielmann, G. A. Reider, P. B. Corkum, F. Krausz, *Science* **2001**, *291*, 1923.

[190] S. Ghimire, A. D. DiChiara, E. Sistrunk, P. Agostini, L. F. DiMauro, D. A. Reis, *Nat. Phys.* **2011**, *7*, 138.

[191] O. Schubert, M. Hohenleutner, F. Langer, B. Urbanek, C. Lange, U. Huttner, D. Golde, T. Meier, M. Kira, S. W. Koch, R. Huber, *Nat. Photonics* **2014**, *8*, 119.

[192] T. T. Luu, M. Garg, S. Y. Kruchinin, A. Moulet, M. T. Hassan, E. Goulielmakis, *Nature* **2015**, *521*, 498.

[193] G. Vampa, T. J. Hammond, M. aucer, X. Ding, X. Ropagnol, T. Ozaki, S. Delprat, M. Chaker, N. Thiré, B. E. Schmidt, F. Légaré, D. D. Klug, A. Yu Naumov, D. M. Villeneuve, A. Staudte, P. B. Corkum, *Nat. Photonics* **2018**, *12*, 465.

[194] T. T. Luu, H. J. WArner, *Nat. Commun.* **2018**, *9*, 916.

[195] G. Vampa, T. J. Hammond, N. Thiré, B. E. Schmidt, F. Légaré, C. R. McDonald, T. Brabec, D. D. Klug, P. B. Corkum, *Phys. Rev. Lett.* **2015**, *115*, 193603.

[196] R. E. F. Silva, A. Jimenez-Galán, B. Amorim, O. Smirnova, M. Ivanov, *Nat. Photonics* **2019**, *13*, 849.

[197] S. A. Mikhailov, *Europhys. Lett.* **2007**, *79*, 27002.

[198] B. Cheng, N. Kanda, T. N. Ikeda, T. Matsuda, P. Xia, T. Schumann, S. Stemmer, J. Itatani, N. P. Armitage, R. Matsunaga, *Phys. Rev. Lett.* **2020**, *124*, 117402.

[199] J. Lim, Y. S. Ang, F. J. García de Abajo, I. Kaminer, L. K. Ang, L. J. Wong, *Phys. Rev. Res.* **2020**, *2*, 043252.

[200] B. Cheng, T. Schumann, Y. Wang, X. Zhang, D. Barbalas, S. Stemmer, N. P. Armitage, *Nano Lett.* **2020**, *20*, 5991.

[201] J. Reimann, S. Schlauderer, C. P. Schmid, F. Langer, S. Baierl, K. A. Kokh, O. E. Tereshchenko, A. Kimura, C. Lange, J. Güdde, U. Höfer, R. Huber, *Nature* **2018**, *562*, 396.

[202] P. Bowlan, E. Martinez-Moreno, K. Reimann, T. Elsaesser, M. Woerner, *Phys. Rev. B* **2014**, *89*, 041408.

[203] N. Yoshikawa, T. Tamaya, K. Tanaka, *Science* **2017**, *356*, 736.

[204] H. A. Hafez, S. Kovalev, J.-C. Deinert, Z. Mics, B. Green, N. Awari, M. Chen, S. Germanskiy, U. Lehnert, J. Teichert, Z. Wang, K.-J. Tielrooij, Z. Liu, Z. Chen, A. Narita, K. Müllen, M. Bonn, M. Gensch, D. Turchinovich, *Nature* **2018**, *561*, 507.

[205] S. Kovalev, R. M. A. Dantas, S. Germanskiy, J.-C. Deinert, B. Green, I. Ilyakov, N. Awari, M. Chen, M. Bawatna, J. Ling, F. Xiu, P. H. M. van Loosdrecht, P. Surówka, T. Oka, Z. Wang, *Nat. Commun.* **2020**, *11*, 2451.

[206] S. Borisenko, Q. Gibson, D. Evtushinsky, V. Zabolotnyy, B. Büchner, R. J. Cava, *Phys. Rev. Lett.* **2014**, *113*, 027603.

[207] A. Akrap, M. Hakl, S. Tchoumakov, I. Crassee, J. Kuba, M. O. Goerbig, C. C. Homes, O. Caha, J. Novák, F. Teppe, W. Desrat, S. Koohpayeh, L. Wu, N. P. Armitage, A. Nateprov, E. Arushanov, Q. D. Gibson, R. J. Cava, D. van der Marel, B. A. Piot, C. Faugeras, G. Martinez, M. Potemski, M. Orlita, *Phys. Rev. Lett.* **2016**, *117*, 136401.

[208] F. Giorgianni, E. Chiadroni, A. Rovere, M. Cestelli-Guidi, A. Perucchi, M. Bellaveglia, M. Castellano, D. Di Giovenale, G. Di Pirro, M. Ferrario, R. Pompili, C. Vaccarezza, F. Villa, A. Cianchi, A. Mostacci, M. Petrarca, M. Brahlek, N. Koirala, S. Oh, S. Lupi, *Nat. Commun.* **2016**, *7*, 11421.

[209] Y. Bai, F. Fei, S. Wang, N. Li, X. Li, F. Song, R. Li, Z. Xu, P. Liu, *Nat. Phys.* **2021**, *17*, 311.

[210] C. P. Schmid, L. Weigl, P. Grössing, V. Junk, C. Gorini, S. Schlauderer, S. Ito, M. Meierhofer, N. Hofmann, D. Afanasiev, J. Crewse, K. A. Kokh, O. E. Tereshchenko, J. Güdde, F. Evers, J. Wilhelm, K. Richter, U. Höfer, R. Huber, *Nature* **2021**, *593*, 385.

[211] R. Matsunaga, N. Tsuji, H. Fujita, A. Sugioka, K. Makise, Y. Uzawa, H. Terai, Z. Wang, H. Aoki, R. Shimano, *Science* **2014**, *345*, 1145.

[212] R. Matsunaga, N. Tsuji, K. Makise, H. Terai, H. Aoki, R. Shimano, *Phys. Rev. B* **2017**, *96*, 020505.

[213] H. Chu, M.-J. Kim, K. Katsumi, S. Kovalev, R. D. Dawson, L. Schwarz, N. Yoshikawa, G. Kim, D. Putzky, Z. Z. Li, H. Raffy, S. Germanskiy, J.-C. Deinert, N. Awari, I. Ilyakov, B. Green, M. Chen, M. Bawatna, G. Cristiani, G. Logvenov, Y. Gallais, A. V. Boris, B. Keimer, A. P. Schnyder, D. Manske, M. Gensch, Z. Wang, R. Shimano, S. Kaiser, *Nat. Commun* **2020**, *11*, 1793.

[214] J.-C. Deinert, D. Alcaraz Iranzo, R. Pérez, X. Jia, H. A. Hafez, I. Ilyakov, N. Awari, M. Chen, M. Bawatna, A. N. Ponomaryov, S. Germanskiy, M. Bonn, F. H. L. Koppens, D. Turchinovich, M. Gensch, S. Kovalev, K.-J. Tielrooij, *ACS Nano* **2020**, *15*, 1145.

[215] S. Patankar, L. Wu, B. Lu, M. Rai, J. D. Tran, T. Morimoto, D. E. Parker, A. G. Grushin, N. L. Nair, J. G. Analytis, J. E. Moore, J. Orenstein, D. H. Torchinsky, *Phys. Rev. B* **2018**, *98*, 165113.

[216] T. Morimoto, N. Nagaosa, *Sci. Adv.* **2016**, *2*, 5.

[217] J. L. Cheng, J. E. Sipe, S. W. Wu, *ACS Photonics* **2020**, *7*, 2515.

[218] C. H. Lee, H. H. Yap, T. Tai, G. Xu, X. Zhang, J. Gong, *Phys. Rev. B* **2020**, *102*, 035138.

[219] C. Zhu, F. Wang, Y. Meng, X. Yuan, F. Xiu, H. Luo, Y. Wang, J. Li, X. Lv, L. He, Y. Xu, J. Liu, C. Zhang, Y. Shi, R. Zhang, S. Zhu, *Nat. Commun.* **2017**, *8*, 14111.

[220] K. Sumida, Y. Ishida, T. Yoshikawa, J. Chen, M. Nurmamat, K. A. Kokh, O. E. Tereshchenko, S. Shin, A. Kimura, *Phys. Rev. B* **2019**, *99*, 085302.

[221] C. P. Weber, B. S. Berggren, M. G. Masten, T. C. Ogloza, S. Deckoff-Jones, J. Madéo, M. K. L. Man, K. M. Dani, L. Zhao, G. Chen, J. Liu, Z. Mao, L. M. Schoop, B. V. Lotsch, S. S. P. Parkin, M. Ali, *J. Appl. Phys.* **2017**, *122*, 223102.

[222] U. Keller, *Nature* **2003**, *424*, 831.

[223] Y. Meng, C. Zhu, Y. Li, X. Yuan, F. Xiu, Y. Shi, Y. Xu, F. Wang, *Opt. Lett.* **2018**, *43*, 1503.

[224] Y. Sun, Y. Meng, H. Jiang, S. Qin, Y. Yang, F. Xiu, Y. Shi, S. Zhu, F. Wang, *Opt. Lett.* **2019**, *44*, 582.

[225] V. Ryzhii, M. Ryzhii, T. Otsuji, *J. Appl. Phys.* **2007**, *101*, 083114.

[226] T. Li, L. Luo, M. Hupalo, J. Zhang, M. C. Tringides, J. Schmalian, J. Wang, *Phys. Rev. Lett.* **2012**, *108*, 167401.

[227] I. Gierz, J. C. Petersen, M. Mitrano, C. Cacho, I. C. E. Turcu, E. Springate, A. Stöhr, A. Köhler, U. Starke, A. Cavalleri, *Nat. Mater.* **2013**, *12*, 1119.

[228] C. J. Docherty, C.-T. Lin, H. J. Joyce, R. J. Nicholas, L. M. Herz, L.-J. Li, M. B. Johnston, *Nat. Commun.* **2012**, *3*, 1228.

[229] A. J. Frenzel, C. H. Lui, Y. C. Shin, J. Kong, N. Gedik, *Phys. Rev. Lett.* **2014**, *113*, 056602.

[230] S. Zhu, Y. Ishida, K. Kuroda, K. Sumida, M. Ye, J. Wang, H. Pan, M. Taniguchi, S. Qiao, S. Shin, A. Kimura, *Sci. Rep.* **2014**, *5*, 13213.

[231] M. Orlita, D. M. Basko, M. S. Zholudev, F. Teppe, W. Knap, V. I. Gavrilenko, N. N. Mikhailov, S. A. Dvoretskii, P. Neugebauer, C. Faugeras, A. L. Barra, G. Martinez, M. Potemski, *Nat. Phys.* **2014**, *10*, 233.

[232] A. Ravid, A. Sher, G. Cinader, A. Zussman, *J. Appl. Phys.* **1993**, *73*, 7102.

[233] S. V. Morozov, V. V. Rumyantsev, M. A. Fadeev, M. S. Zholudev, K. E. Kudryavtsev, A. V. Antonov, A. M. Kadykov, A. A. Dubinov, N. N. Mikhailov, S. A. Dvoretsky, V. I. Gavrilenko, *Appl. Phys. Lett.* **2017**, *111*, 192101.

[234] D. B. But, M. Mittendorff, C. Consejo, F. Teppe, N. N. Mikhailov, S. A. Dvoretskii, C. Faugeras, S. Winnerl, M. Helm, W. Knap, M. Potemski, M. Orlita, *Nat. Photonics* **2019**, *13*, 783.

[235] H. Aoki, *Appl. Phys. Lett.* **1986**, *48*, 559.

[236] A. N. Afanasiev, A. A. Greshnov, D. Svintsov, *Phys. Rev. B* **2019**, *99*, 115202.

[237] W. Lu, J. Ling, F. Xiu, D. Sun, *Phys. Rev. B* **2018**, *98*, 104310.

[238] W. Zhang, Y. Yang, P. Suo, W. Zhao, J. Guo, Q. Lu, X. Lin, Z. Jin, L. Wang, G. Chen, F. Xiu, W. Liu, C. Zhang, G. Ma, *Appl. Phys. Lett.* **2019**, *114*, 221102.

[239] C. Qian, C. Yu, S. Jiang, T. Zhang, J. Gao, S. Shi, H. Pi, H. Weng, R. Lu, *arXiv:2106.14263*, **2021**.

[240] N. Kumar, S. N. Guin, K. Manna, C. Shekhar, C. Felser, *Chem. Rev.* **2020**, *121*, 2780.

Shanhui Fan is the Joseph and Hon Mai Goodman Professor in the School of Engineering at Stanford University. He is a Professor of Electrical Engineering, a Professor of Applied Physics (by courtesy), and a Senior Fellow in the Precourt Institute for Energy. He is also a faculty member of the Edward L. Ginzton Laboratory, for which he was the Director from 2014 to 2021. His research interests are in fundamental studies of nanophotonic structures, especially photonic crystals and meta-materials, and applications of these structures in energy and information technology applications.

Ryusuke Matsunaga is an Associate Professor in The Institute for Solid State Physics (ISSP), The University of Tokyo, Japan. He obtained his Ph.D. from Kyoto University in 2011. He served as an Assistant Professor at Department of Physics, Faculty of Science, The University of Tokyo from 2011 to 2017 and an Associate Professor in ISSP since 2017. His research involves experimental studies of light-matter interaction and ultrafast phenomena in a variety of materials, such as topological semimetals, magnetic materials, semiconductors, and superconductors, especially in infrared and terahertz frequency range.